



















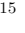


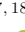


















## The rise of the galactic empire: luminosity functions at $z \sim 17$ and $z \sim 25$ estimated with the MIDIS+NGDEEP ultra-deep JWST/NIRCam dataset

PABLO G. PÉREZ-GONZÁLEZ <sup>1</sup>, GÖRAN ÖSTLIN <sup>2</sup>, LUCA COSTANTIN <sup>1</sup>, JENS MELINDER <sup>2</sup>,  
STEVEN L. FINKELSTEIN <sup>3</sup>, RACHEL S. SOMERVILLE <sup>4</sup>, MARIANNA ANNUNZIATELLA <sup>1</sup>, JAVIER ÁLVAREZ-MÁRQUEZ <sup>1</sup>,  
LUIS COLINA <sup>1</sup>, AVISHAI DEKEL <sup>5</sup>, HENRY C. FERGUSON <sup>6</sup>, ZHAOZHOU LI <sup>5</sup>, L. Y. AARON YUNG <sup>6</sup>,  
MICAELA B. BAGLEY <sup>7,8</sup>, LEINDERT A. BOOGAARD <sup>9</sup>, DENIS BURGARELLA <sup>10</sup>, ANTONELLO CALABRÒ <sup>11</sup>,  
KARINA I. CAPUTI <sup>12,13</sup>, YINGJIE CHENG <sup>14</sup>, ANDREAS ECKART <sup>15</sup>, MAURO GIAVALISCO <sup>14</sup>, STEVEN GILLMAN <sup>16,17</sup>,  
THOMAS R. GREVE <sup>16,17,18</sup>, NIMISH P. HATHI <sup>6</sup>, JENS HJORTH <sup>19</sup>, MARC HUERTAS-COMPANY <sup>20,21,22,23</sup>,  
JEYHAN S. KARTALTEPE <sup>24</sup>, ANTON M. KOEKEMOER <sup>6</sup>, VASILY KOKOREV <sup>3</sup>, ÁLVARO LABIANO <sup>25</sup>,  
DANIAL LANGEROODI <sup>19</sup>, GENE C. K. LEUNG <sup>26</sup>, PRIYAMVADA NATARAJAN <sup>27</sup>, CASEY PAPOVICH <sup>28,29</sup>,  
FLORIAN PEISSKER <sup>30</sup>, LAURA PENTERICCI <sup>11</sup>, NOR PIRZKAL <sup>31</sup>, PIERLUIGI RINALDI <sup>32</sup>, PAUL VAN DER WERF <sup>9</sup>,  
AND FABIAN WALTER <sup>33</sup>

<sup>1</sup>Centro de Astrobiología (CAB), CSIC-INTA, Ctra. de Ajalvir km 4, Torrejón de Ardoz, E-28850, Madrid, Spain

<sup>2</sup>Department of Astronomy, Stockholm University, Oscar Klein Centre, AlbaNova University Centre, 106 91 Stockholm, Sweden

<sup>3</sup>Department of Astronomy, The University of Texas at Austin, Austin, TX 78712, USA

<sup>4</sup>Center for Computational Astrophysics, Flatiron Institute, 162 5th Avenue, New York, NY, 10010, USA

<sup>5</sup>Racah Institute of Physics, The Hebrew University of Jerusalem, Jerusalem 91904, Israel

<sup>6</sup>Space Telescope Science Institute, 3700 San Martin Drive, Baltimore, MD 21218, USA

<sup>7</sup>Department of Astronomy, The University of Texas at Austin, Austin, TX, USA

<sup>8</sup>Astrophysics Science Division, NASA Goddard Space Flight Center, 8800 Greenbelt Rd, Greenbelt, MD 20771, USA

<sup>9</sup>Leiden Observatory, Leiden University, PO Box 9513, 2300 RA Leiden, The Netherlands

<sup>10</sup>Aix Marseille Université, CNRS, CNES, LAM, Marseille, France

<sup>11</sup>INAF Osservatorio Astronomico di Roma, Via Frascati 33, 00078 Monte Porzio Catone, Rome, Italy

<sup>12</sup>Kapteyn Astronomical Institute, University of Groningen, P.O. Box 800, 9700AV Groningen, The Netherlands

<sup>13</sup>Cosmic Dawn Center (DAWN), Copenhagen, Denmark

<sup>14</sup>University of Massachusetts Amherst, 710 North Pleasant Street, Amherst, MA 01003-9305, USA

<sup>15</sup>I. Physikalisches Institut der Universität zu Köln, Zùlpicher Str. 77, 50937 Köln, Germany

<sup>16</sup>Cosmic Dawn Center (DAWN), Denmark

<sup>17</sup>DTU Space, Technical University of Denmark, Elektrovej, Building 328, 2800, Kgs. Lyngby, Denmark

<sup>18</sup>Dept. of Physics and Astronomy, University College London, Gower Street, London WC1E 6BT, United Kingdom

<sup>19</sup>DARK, Niels Bohr Institute, University of Copenhagen, Jagtvej 155A, 2200 Copenhagen, Denmark

<sup>20</sup>Instituto de Astrofísica de Canarias (IAC), La Laguna, E-38205, Spain

<sup>21</sup>Universidad de La Laguna. Avda. Astrofísico Fco. Sanchez, La Laguna, Tenerife, Spain

<sup>22</sup>Observatoire de Paris, LERMA, PSL University, 61 avenue de l'Observatoire, F-75014 Paris, France

<sup>23</sup>Université Paris-Cité, 5 Rue Thomas Mann, 75014 Paris, France

<sup>24</sup>Laboratory for Multiwavelength Astrophysics, School of Physics and Astronomy, Rochester Institute of Technology, 84 Lomb Memorial Drive, Rochester, NY 14623, USA

<sup>25</sup>Telespazio UK for the European Space Agency, ESAC, Camino Bajo del Castillo s/n, 28692 Villanueva de la Cañada, Spain

<sup>26</sup>MIT Kavli Institute for Astrophysics and Space Research, 77 Massachusetts Ave., Cambridge, MA 02139, USA

<sup>27</sup>Department of Astronomy, Yale University, New Haven, CT 06511, USA; Department of Physics, Yale University, New Haven, CT 06520, USA; Black Hole Initiative, Harvard University, 20 Garden Street, Cambridge, MA 02138, USA

<sup>28</sup>Department of Physics and Astronomy, Texas A&M University, College Station, TX, 77843-4242 USA

<sup>29</sup>George P. and Cynthia Woods Mitchell Institute for Fundamental Physics and Astronomy, Texas A&M University, College Station, TX, 77843-4242 USA

<sup>30</sup>(I. Physikalisches Institut der Universität zu Köln, Zùlpicher Str. 77, 50937 Köln, Germany

<sup>31</sup>ESA/AURA Space Telescope Science Institute

<sup>32</sup>Steward Observatory, University of Arizona, 933 North Cherry Avenue, Tucson, AZ 85721, USA

<sup>33</sup>Max Planck Institut für Astronomie, Königstuhl 17, D-69117, Heidelberg, Germany

ABSTRACT

We present a sample of six F200W and three F277W dropout sources identified as  $16 < z < 25$  galaxy candidates based on the deepest JWST/NIRCam data to date, provided by the MIRI Deep Imaging Survey (MIDIS) and the Next Generation Deep Extragalactic Exploratory Public survey (NGDEEP), reaching  $5\sigma$  depths of  $\sim 31.5$  mag (AB) at  $\geq 2 \mu\text{m}$ . We estimate ultraviolet (UV) luminosity functions and densities at  $z \sim 17$  and  $z \sim 25$ . We find that the number density of galaxies with absolute magnitudes  $-19 < M_{\text{UV}} < -18$  (AB) at  $z \sim 17$  ( $z \sim 25$ ) is a factor of 4 (25) smaller than at  $z \sim 12$ ; a similar evolution is observed for the luminosity density. Compared to state-of-the-art galaxy simulations, we find the need for an enhanced UV-photon production at  $z = 17 - 25$  in  $M_{\text{DM}} = 10^{8.5-9.5} M_{\odot}$  dark matter halos, maybe provided by an increase in the star formation efficiency at early times and/or by intense bursts fed by very low metallicity or primordial gas. There are few robust theoretical predictions for the evolution of galaxies above  $z \sim 20$  in the literature, however, the continuing rapid drop in the halo mass function suggests more rapid evolution than we observe if photon production efficiencies remained constant. Our  $z > 16$  galaxy candidates present mass-weighted ages around 30 Myr, and attenuations  $A(V) < 0.1$  mag. Their average stellar mass is  $M_{\star} \sim 10^7 M_{\odot}$ , implying a star formation efficiency (stellar-to-baryon mass fraction) around 10%. We find three galaxies with very blue UV spectral slopes ( $\beta \sim -3$ ) compatible with low metallicity or Pop III and young ( $\lesssim 10$  Myr) stars and/or high escape fractions of ionizing photons, the rest presenting slopes  $\beta \sim -2.5$  similar to  $z = 10 - 12$  samples.

*Keywords:* Galaxy formation (595) — Galaxy evolution (594) — early universe (435) — High-redshift galaxies (734) — Broad band photometry (184) — JWST (2291)

## 1. INTRODUCTION

After almost three years of scientific operations of JWST, there is a consensus on the analysis of the  $z > 10$  Universe performed with a variety of datasets (see [Adamo et al. 2024](#) for a review) indicating that the Universe was more active in the formation of galaxies during the first half billion years ( $z > 9$ ) than anticipated based on empirical extrapolations of pre-JWST observations at lower redshifts, as well as the predictions of state-of-the-art physics-based simulations that were calibrated to match pre-JWST observations ([Adams et al. 2024](#); [Castellano et al. 2022, 2023](#); [Conselice et al. 2024](#); [Donnan et al. 2024, 2023](#); [Finkelstein et al. 2022, 2023, 2024](#); [Hainline et al. 2024a](#); [Harikane et al. 2023](#); [Leung et al. 2023](#); [McLeod et al. 2024](#); [Pérez-González et al. 2023a](#); [Robertson et al. 2024](#); [Yan et al. 2023c](#); [Willott et al. 2024](#)).

Virtually all surveys reaching different depths, exploring different sky regions with deep, small areas as well as shallow, large area strategies, and with different filter sets (e.g. CEERS: [Finkelstein et al. 2025](#); PRIMER: [Donnan et al. 2024](#); NGDEEP: [Bagley et al. 2024](#); COSMOS-Web: [Casey et al. 2023](#), JADES: [Eisenstein et al. 2023](#); [Rieke et al. 2023](#); MIDIS: [Östlin et al. 2024](#), UNCOVER: [Bezanson et al. 2024](#)), find numerous  $z > 9$  galaxy candidates, in excess of expectations. Many of these candidates have been validated spectroscopically ([Arrabal Haro et al. 2023a,b](#); [Curtis-Lake et al. 2023](#); [Castellano et al. 2024](#); [Harikane et al. 2024](#); [Carniani](#)

[et al. 2024](#)). The cumulative number density of high redshift galaxies at the bright end of the luminosity function (apparent magnitudes brighter than F277W  $\sim 29$ , typically probing an order of magnitude fainter than  $L^*$  at  $z \sim 12$ ) exceed expectations from pre-JWST simulations by a factor of 10 at  $z \sim 9$  and nearly a factor of 100 up to  $z \sim 12$  (see, e.g., [Finkelstein et al. 2023, 2024](#); [Pérez-González et al. 2023a](#)).

Probing redshifts higher than  $z \sim 12$  in both photometrically selected candidate samples and spectroscopic follow-up campaigns remains very challenging, although some efforts exist (apart from references above, see [Yan et al. 2023a](#); [Kokorev et al. 2024](#)). From the photometric point of view, hundreds of F150W dropouts have been selected and many confirmed with spectroscopy. But no F200W dropout galaxy has been confirmed, the closest being the highest confirmed redshift source known, JADES-GS-z14-0 ([Robertson et al. 2024](#); [Carniani et al. 2024](#)), which only disappears bluewards of  $\sim 1.8 \mu\text{m}$ . Interestingly, several  $z > 14$  relatively bright F200W dropouts selected as photometric candidates have also been confirmed to instead be low redshift interlopers, typically dusty galaxies at  $z = 4 - 5$  ([Naidu et al. 2022](#); [Zavala et al. 2023](#); [Pérez-González et al. 2023b](#); [Arrabal Haro et al. 2023a](#)). Overall, our statement about the consensus in the results obtained out to  $z \sim 12$  and their reliability, based on relatively large photometric samples and a statistically meaningful number of spectroscopic confirmations, cannot yet be extended to  $z \gtrsim 12$ .

Part of the lack of consensus, apart from the very few spectroscopic confirmations beyond  $z \sim 12$  (only 5 galaxies, see references in Figure 1), comes from the limited depth of NIRC*am* datasets in the relevant filters needed to detect galaxies in the first 350 Myr of the Universe. Two points have to be taken into account to understand the existence of the current redshift frontier at  $z \sim 12$ . First, photometric samples typically reach magnitudes around F277W $\sim$ 29, consistent with the aim to detect Lyman breaks of at least 1.0-1.5 mag and considering that most surveys are limited to magnitude 30.5 in the filters longwards of  $2 \mu\text{m}$  (even the deepest such as NGDEEP and JADES/JOF). Second, most of the spectroscopically confirmed  $z > 9$  galaxies (see caption of Figure 1 for references) have magnitudes around F277W $\sim$ 28 (one mag up or down), with a significant number of them having been assigned a redshift based on low spectral resolution NIRSpec prism data probing the continuum emission and the Lyman break rather than detecting (the typically quite faint) ultraviolet emission lines.

In this paper, we aim to construct a robust sample of  $z > 16$  galaxies by identifying F200W and F277W dropouts (probing roughly  $16 < z < 21$  and  $24 < z < 28$ , respectively) in the deepest dataset obtained by JWST with its NIRC*am* instrument to date. This dataset results from combining the data from: (1) the parallel field of the MIRI Deep Survey (MIDIS, Östlin et al. 2024), and its red extension (MIDIS-RED), whose primary observations were carried out in the HUDF with MIRI for nearly 100 hours; and (2) the Next Generation Deep Extragalactic Exploratory Public survey (NGDEEP), which observed the HUDF with NIRISS as prime for 60 hours (Bagley et al. 2024). The combination of these two surveys in all NIRC*am* broad bands from  $2 \mu\text{m}$  redwards (i.e., F200W, F277W, F356W, and F444W) in the parallel field located to the SW of the HUDF provides a unique dataset that reaches up to  $\times 2.5$  fainter fluxes than other small-area deep surveys such as JADES or GLIMPSE, and  $\times 10$  times fainter fluxes compared to large-area shallow surveys such as CEERS or PRIMER.

This paper is organized as follows. Section 2 presents our dataset, the NIRC*am* parallels of MIDIS and NGDEEP, and describes our method to select F200W and F277W dropout sources and identify  $z \sim 17$  and  $z \sim 25$  galaxy candidates. The sample is then used to construct UV luminosity functions and derive the early evolution of the luminosity density in the Universe, that are presented in Section 3. In this same section, we provide calculations of the efficiency of production of UV photons by dark matter halos, and discuss the stellar

masses and UV spectral slopes of our candidates. Section 4 summarizes our findings.

Throughout this paper, we assume a flat cosmology with  $\Omega_M = 0.3$ ,  $\Omega_\Lambda = 0.7$ , and a Hubble constant  $H_0 = 70 \text{ km s}^{-1} \text{ Mpc}^{-1}$ . We use AB magnitudes (Oke & Gunn 1983). All stellar mass estimates assume a universal Chabrier form (Chabrier 2003) stellar initial mass function (IMF), unless stated otherwise.

## 2. SELECTION OF $z > 16$ GALAXY CANDIDATES

### 2.1. Data

In this paper, we combine the NIRC*am* data coming from MIDIS (PID 1283, Östlin et al. 2024), extended to MIDIS-RED (PID 6511, Östlin et al. 2025, in prep.) with the observations obtained by NGDEEP (program ID 2079, Bagley et al. 2024). These surveys observed a region located to the SE of the HUDF with a single NIRC*am* pointing and different position angles, each program eventually employing slightly different central coordinates and orientations. For this work, we cut the full observed field of view to the area in common between all NIRC*am* filters (namely, F115W, F150W, F200W, F277W, F356W, and F444W), combining the regions covered by MIDIS and NGDEEP, which adds up  $17.6 \text{ arcmin}^2$  (i.e., around 10% smaller than 2 NIRC*am* pointings).

The raw data were downloaded from the Mikulski Archive for Space Telescopes (MAST) at the Space Telescope Science Institute, and calibrated with the Rainbow pipeline, a bespoke version of the official `rwst` pipeline which includes additional steps to homogenize the background and remove artifacts to be able to achieve the deepest flux levels. The core of the Rainbow pipeline for this paper resides in the `rwst` pipeline, version v1.16.0, `pmap 1298` for the reduction used in this paper. As an addition to that official reduction, we also applied a superbackground homogenization algorithm prior to obtaining the final mosaics, which takes care of background features such as wisps and  $1/f$ -noise removal. As explained by Pérez-González et al. (2024) and Östlin et al. (2024) for MIRI data, for each stage 2 image that needs to be calibrated, we build a median background frame with all the other images taken with the same detector (after masking objects), properly scaled to the median background of the image being reduced. In order to improve the overall background characterization, we create extended masks of every source in the field using a `NoiseChisel` (Akhlaghi & Ichikawa 2015; Golini et al. 2024) run on initial mosaics obtained directly from the official pipeline, and improve the masks with two extra mosaic-building iterations. We customize our setup in order to mask the faintest sources, the dif-

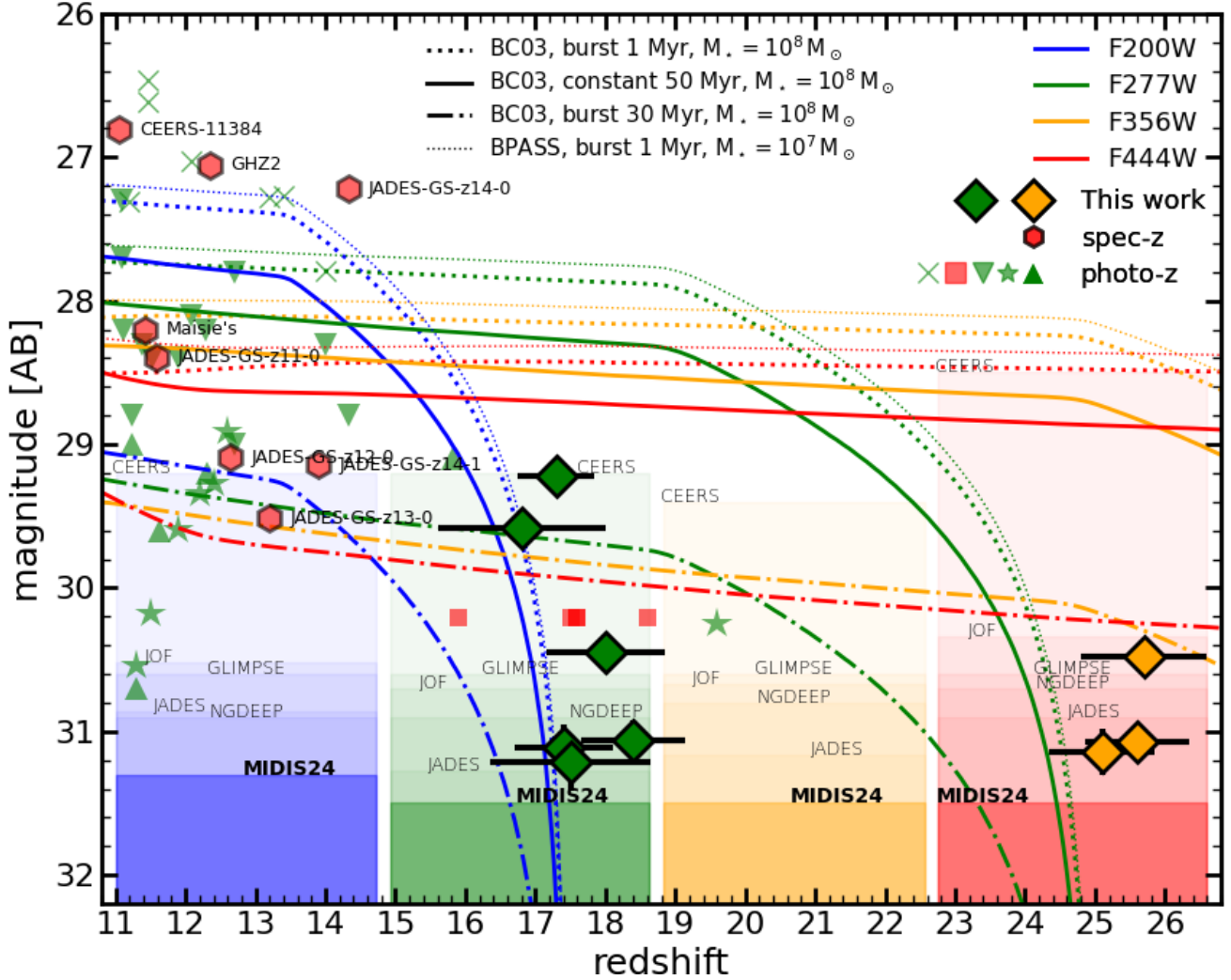


**Figure 1.** Compilation of spectroscopically confirmed galaxies (red hexagons, Arrabal Haro et al. 2023a; Curtis-Lake et al. 2023; Castellano et al. 2024; Carniani et al. 2024) and photometric samples (including Leung et al. 2023 -green pointing-up triangles-, Finkelstein et al. 2024 -pointing-down triangle-, Pérez-González et al. 2023a -green stars-, Kokorev et al. 2024 -red squares-, and Casey et al. 2024 -green crosses-) of galaxies at  $z > 11$ . The  $16 < z < 25$  galaxy candidates presented in this work are plotted with green and orange diamonds, the color representing the band used in the plot, the one closer to and redward of the Lyman break. We also show their magnitude and photometric redshift uncertainties. Lines show the expected magnitudes as a function of redshift of a very young (1 Myr old) starburst with stellar mass  $M_* = 10^8 M_\odot$  according to the Bruzual & Charlot (2003) models (thick dotted line) and a less massive  $M_* = 10^7 M_\odot$  starburst according to the Eldridge et al. (2017) BPASS models (thin dotted line). The expected magnitudes for a more extended star formation history (50 Myr constant star formation population) and a dormant galaxy (which experienced an instantaneous burst 30 Myr before the observation) are also shown (thick continuous and dashed-dotted lines, respectively). All models assume no dust. Shaded regions show the  $5\sigma$  depths of the major galaxy surveys used in the identification of  $z > 11$  galaxy candidates. The darkest regions refer to the dataset used in this paper (MIDIS24, which stands for the 2024 depth, including NGDEEP). The color for all data points, lines, and shaded regions indicates the NIRCcam band considered.

fuse light from galaxy outskirts, and the spikes of the brightest stars.

To optimize the results, and given that wisps changed within our dataset, we only used the images taken within 2 months of each other to build the superbackground frame, also disregarding the short exposures (noisier than the rest) taken for each filter by the NGDEEP pro-

gram (corresponding to when the primary instrument NIRISS was taking imaging data instead of deep grism observations). We found that the superbackground procedure improves the detectability of faint sources in the final mosaics by 0.3-0.4 mag, compared to a more classical background homogenization algorithm based on row, column, and box filtering.

The whole dataset was registered to the same World Coordinate System (WCS) reference frame using the Hubble Legacy Field (HLF) catalog of Whitaker et al. (2019), based on Gaia DR1.2 (Gaia Collaboration et al. 2016a, Gaia Collaboration et al. 2016b). For that purpose, we used the version of the *tweakreg* package published by the CEERS Team (Bagley et al. 2023), switching this task off in stage 3 of the pipeline. All images were drizzled to the same plate scale, namely, 0.03 arcsec/pixel. All images were PSF-matched to the reddest filter (F444W).

The depths of the NIRCcam dataset used in this paper reaches maximum magnitude  $5\sigma$  limits for point-like sources of 30.9 to 31.5 in all filters for the region with maximum overlap, and using  $0.1''$  circular apertures corrected for PSF effects (i.e., to total magnitudes assuming point-like sources). The depth in the area covered only by MIDIS or NGDEEP alone degrades by up to 0.5 mag in some filters. Special mention must be made of the three reddest bands, all reaching magnitudes beyond 31.1 in the full considered area, essential to select F200W dropouts (the two reddest to select F277W dropouts) down to  $\sim 31$  mag, significantly improving previous observational efforts (see Figure 1). These selection limits are still adequate, with our limiting magnitudes in the dropout band, to detect the intense breaks (1.0-1.5 mag for the mentioned magnitude limit), most probably corresponding to the Lyman break.

The actual areas, exposure times, and depths found in different regions of the combined field of view are given in Table 1. We note that MIDIS-red is supposed to further increase the exposure time in short-wavelength (SW) and long-wavelength (LW) filters in the late Fall of 2025.

The depths of the data used in this work are shown in Figure 1, compared to other surveys and presenting several samples of  $z > 11$  galaxies selected photometrically and also those confirmed spectroscopically. We also present the newly discovered  $z > 16$  galaxy candidates reported in this paper.

## 2.2. Source detection and photometry

Source detection was carried out with Source Extractor (Bertin & Arnouts 1996), executed on cold and hot modes to properly deal with the brightest extended galaxies as well as the faintest small sources (Rix et al. 2004). Detection was carried out in the F277W, F356W, and F444W filters, as well as in the stack of the three bands and stacks combining two of them, all obtained with constant weights. The different catalogs were cross-correlated with each other and a master list of sources

**Table 1.** Characteristics of the MIDIS+NGDEEP NIRCcam datasets.

Filter	$5\sigma$ depth (time)		
	MIDIS+NGDEEP	MIDIS	NGDEEP
F115W	31.1 (226 ks)	30.6 (55 ks)	31.0 (171 ks)
F150W	30.9 (138 ks)	30.4 (58 ks)	30.7 (80 ks)
F200W	31.3 (197 ks)	31.3 (166 ks)	30.6 (31 ks)
F277W	31.5 (135 ks)	31.5 (55 ks)	31.2 (80 ks)
F356W	31.5 (119 ks)	31.3 (58 ks)	31.1 (62 ks)
F444W	31.5 (321 ks)	31.3 (166 ks)	31.3 (155 ks)

NOTE—Table with information for all filters used in this work. We show the  $5\sigma$  depths corresponding to a point-like source measured in a  $0.2''$  diameter circular aperture and corrected for the limited aperture using empirical PSFs. The three columns stand for the depth of the MIDIS+NGDEEP, MIDIS-only, and NGDEEP-only areas, extending for 2.8, 3.4, and 11.4 arcmin<sup>2</sup>, respectively, for a total area considered in this paper of 17.6 arcmin<sup>2</sup>.

was constructed by keeping all individual detections separated by more than  $0.15''$  from any other source. The parent catalog is composed of 110,125 sources, detected in 17.6 arcmin<sup>2</sup>.

Integrated photometry was measured for the parent catalog in Kron (1980) apertures, assuming Kron factors of 2.5 for the cold SExtractor execution, and 1.1 for the hot one. Aperture photometry was also measured in circular apertures of diameter  $0.2''$ ,  $0.3''$ , and  $0.4''$ , applying aperture corrections for point-like sources, and scaling the final photometry with a constant factor obtained by averaging the flux ratios with respect to the the Kron aperture in a source by source basis. In this paper, given that we are interested in very high redshift faint sources, we used the  $0.2''$  diameter aperture photometry for our fiducial spectral energy distributions, but evaluated the results with all four different photometric values (i.e., the direct Kron aperture and the three circular aperture photometries).

Uncertainties in the flux measurements for each source and band were calculated by measuring the background noise locally with a procedure presented by Pérez-González et al. (2008) and also used by Pérez-González et al. (2023b, where a more quantitative characterization of the method is presented), devised to take into account correlated noise. Briefly, we built artificial apertures composed of randomly-selected non-contiguous pixels (in fact, separated by more than 3 pixels from any other entering the statistics calculation) in the neighborhood of each source, adding up the number of pixels of the photometric aperture whose uncertainty we were trying to estimate. The whole procedure ensures that all the pixels included in the noise calculation are independent, and not affected by correlated noise.

### 2.3. Selection method

The selection of high redshift galaxy candidates follows the same method used by Pérez-González et al. (2023b), adopted from other works such as Finkelstein et al. (2023) and Harikane et al. (2023). First, we selected all galaxies whose median flux, averaged across all four spectral energy distributions (SEDs), i.e., the SEDs derived from the Kron aperture and the three circular apertures, and using the F277W, F356W, and F444W filters, had a  $\text{SNR} > 5$ . This sample has an median and quartiles F444W magnitudes of  $30.3 \pm 1.4$ . Then, in order to select dropouts and to make them compatible with  $z > 16$ , which would mean zero flux blue-wards of the Lyman break, we restricted the catalog to all sources with a median  $\text{SNR} < 3$  in F115W and F150W, as well as F200W and F277W separately, resulting in a sample with average F444W magnitudes  $31.3 \pm 0.6$  and  $31.4 \pm 0.7$  for the F200W and F277W dropouts (5633 and 386 sources, respectively), respectively.

After the observational cuts, we analyzed the SEDs of the dropout galaxies to obtain photometric redshifts and other physical properties. Two independent codes were used for this purpose. First, we used the `eazy` code (Brammer et al. 2008) with the default FSPS templates (Conroy & Gunn 2010), adding a dusty galaxy template (Muzzin et al. 2013) and the templates presented by Larson et al. (2022) to optimize the analysis of high-redshift galaxies, which include emission-line galaxies with high equivalent widths (known to contaminate *JWST* high-redshift samples, see Zavala et al. 2022 and Naidu et al. 2022). We also used two templates with extreme equivalent width emission lines, one presented by Erb et al. (2010), the other based on the most extreme galaxy identified by Trump et al. (2023). Finally, new obscured Active Galactic Nucleus (AGN) and stellar+AGN little red dot (LRD) templates from Killi et al. (2023) and Pérez-González et al. (2024) were also added. We did not use any magnitude prior nor a template error, allowing the redshift to take values between  $z = 0$  and  $z = 35$ .

Photometric redshifts were also estimated with `prospector` (Johnson et al. 2021), using FSPS templates with python bindings (Conroy & Gunn 2010; Foreman-Mackey et al. 2014) and the `dynesty` nested sampler (Speagle 2020). For this fitting, we fitted for four free parameters: redshift  $z$ , stellar mass  $M_*$ , dust attenuation  $E(B-V)$ , and stellar population age. We assumed a parametric star formation history (delayed  $\tau$  model), and intergalactic medium (IGM) absorption turned on. The stellar (and gas) metallicity was fixed

at  $0.03 Z_\odot$  and all other parameters fixed at their FSPS default values (e.g., the SFH timescale was set to an e-folding time of  $\tau = 1$  Gyr). We used uniform priors on  $z \in [2.0, 31.0]$ ,  $\log M_* \in [6, 10]$ , stellar age between 1 Myr and age of the Universe at the given  $z$ , and a prior on  $E(B-V)$  in the shape of a normal distribution centered and truncated at 0.0 with a standard deviation of 0.3.

We obtained photometric redshift probability distribution functions (zPDFs) with both codes using the SEDs for the four different apertures mentioned in Section 2.1. The zPDFs were then analyzed to build a sample of  $z \gtrsim 16$  galaxy candidates.

Based on photometric redshifts, we further cut the original sample to those galaxies presenting a most probable (as found by integrating the zPDF) and the peak (that providing the smallest  $\chi^2$  value) redshift above  $z > 10$ , keeping only those galaxies with a  $> 70\%$  cumulative probability of lying at  $z > 15$ . The final cut was on  $\chi^2$  values, ensuring that the difference between the minimum value of the zPDF at  $z < 10$  and  $z > 10$ ,  $\Delta \log \chi^2$ , was larger than 0.4 dex. In the final sample that we used to estimate luminosity functions (see the following section), we only kept candidates for which all apertures and the two codes provided photometric results compatible with  $z > 10$ .

This sample of 733 sources selected with observational and physical criteria were also inspected visually. We vetted galaxies unaffected by artifacts such as star spikes and/or contamination by nearby objects, as well as sources for which stacks of the SW data provided  $\text{SNR} > 2$  measurements in any of the photometric apertures.

Our final sample is composed of six F200W dropouts and three F277W dropouts, whose typical photometric redshifts are  $z \sim 17$  and  $z \sim 25$ , respectively. The sample is presented in Table 2.

### 2.4. Candidates

In this section, we present the candidates identified with our selection method that survived the vetting process, both procedures described in the previous subsection.

Figure 1 presented this sample (red diamonds). The bulk of our sample has F444W magnitudes between 30 and 31.5 mag, a brightness level that lies more than 1 magnitude beyond the depths achieved by prior medium area shallow surveys such as CEERS. The magnitudes are comparable to the  $5\sigma$  depths obtained by the deepest surveys carried out in 2022-2024, such as JADES or NGDEEP. The two brightest objects in our sample are comparable to the  $z \sim 17$  candidates presented by

**Table 2.** Galaxy candidates at  $16 < z < 25$  selected with the MIDIS+NGDEEP dataset.

MIDIS ID	Galaxy name	RA (J2000)	DEC (J2000)	F115W	F150W	F200W	F277W	F356W	F444W
		[degrees]	[degrees]	[mag]	[mag]	[mag]	[mag]	[mag]	[mag]
$z \sim 17$ sample									
midisred0006800	MIDIS-z17-1	53.28551340	-27.87947000	> 32.1	> 32.2	> 32.7	31.06 ± 0.15	31.26 ± 0.16	31.19 ± 0.16
midisred0019207	MIDIS-z17-2	53.27974630	-27.86530520	> 32.4	> 31.7	> 32.4	31.11 ± 0.16	31.84 ± 0.29	31.52 ± 0.19
midisred0028033	MIDIS-z17-3	53.30680240	-27.85571070	> 31.1	> 31.4	> 33.0	29.22 ± 0.05	30.12 ± 0.07	31.41 ± 0.14
midisred0047123	MIDIS-z17-4	53.23560300	-27.81536380	> 32.7	> 32.3	> 31.6	30.45 ± 0.11	30.60 ± 0.12	30.73 ± 0.16
midisred0051552	MIDIS-z17-5	53.25235830	-27.80295390	> 32.2	> 31.6	> 31.6	30.77 ± 0.13	30.76 ± 0.18	31.01 ± 0.18
midisred0053786	MIDIS-z17-6	53.24822550	-27.79413320	> 32.4	> 30.3	> 30.4	29.58 ± 0.06	29.89 ± 0.15	29.63 ± 0.07
$z \sim 24$ sample									
midisred0019248	MIDIS-z25-1	53.23226140	-27.86526940	> 32.6	> 32.3	> 33.0	> 32.4	30.48 ± 0.10	30.60 ± 0.25
midisred0048457	MIDIS-z25-2	53.23122790	-27.81162440	> 32.5	> 31.9	> 32.3	> 33.0	31.14 ± 0.16	31.83 ± 0.43
midisred0049147	MIDIS-z25-3	53.23929800	-27.80989420	> 33.0	> 31.6	> 32.3	> 33.0	31.07 ± 0.11	31.12 ± 0.14

NOTE—We provide coordinates and magnitudes in all NIRCcam bands, identifying each galaxy by its MIDIS parent catalog ID and the galaxy name chosen for this paper about  $z > 16$  galaxy candidates. Upper limits refer to  $1-\sigma$ .

Kokorev et al. (2024) using GLIMPSE data and with several spectroscopically confirmed  $z \gtrsim 13$  galaxies (see Fig. 1 caption for references).

Comparing the magnitudes with the models depicted in Figure 1, we infer that the stellar masses for our  $z > 16$  galaxy candidates are nearly an order of magnitude smaller than the average of the spectroscopically confirmed galaxies at  $11 < z < 14.5$ , i.e., their stellar masses should be around  $10^{7-8} M_{\odot}$  (where the BPASS simple stellar population models suggest an order of magnitude smaller stellar masses than BC03). We expect 0.3-0.4 dex variations depending on the star formation history. We will discuss the stellar mass estimates of our selected galaxies further in Section 3.4.

Figure 2 shows color-color plots for the parent sample and our  $z \sim 17$  and  $z \sim 25$  galaxy candidates. We remark that our selection is based on break detection and photometric redshifts, not directly colors, but we compare with color-color criteria in this figure. We plot the color tracks as a function of redshift for various galaxy types previously detected by JWST at high redshift, including a template for a galaxy with a very recent starburst (1 Myr old); a dormant galaxy with a 30 Myr old star formation event; an LRD; and a dusty star-forming galaxy, which is the typical interloper in the search for  $z > 8$  galaxy candidates (see Zavala et al. 2023 or Naidu et al. 2022). All our  $z \gtrsim 16$  galaxy candidates have colors redder than 1.5 mag, implying the presence of a strong break, most probably identified with the Lyman and not the Balmer one, as shown by the selection locus presented by Castellano et al. (2023) and Kokorev et al. (2024) and marked in the figure. Remarkably, we detect two F200W dropout galaxies and one F277W with very blue colors in the bands probing the far-UV spec-

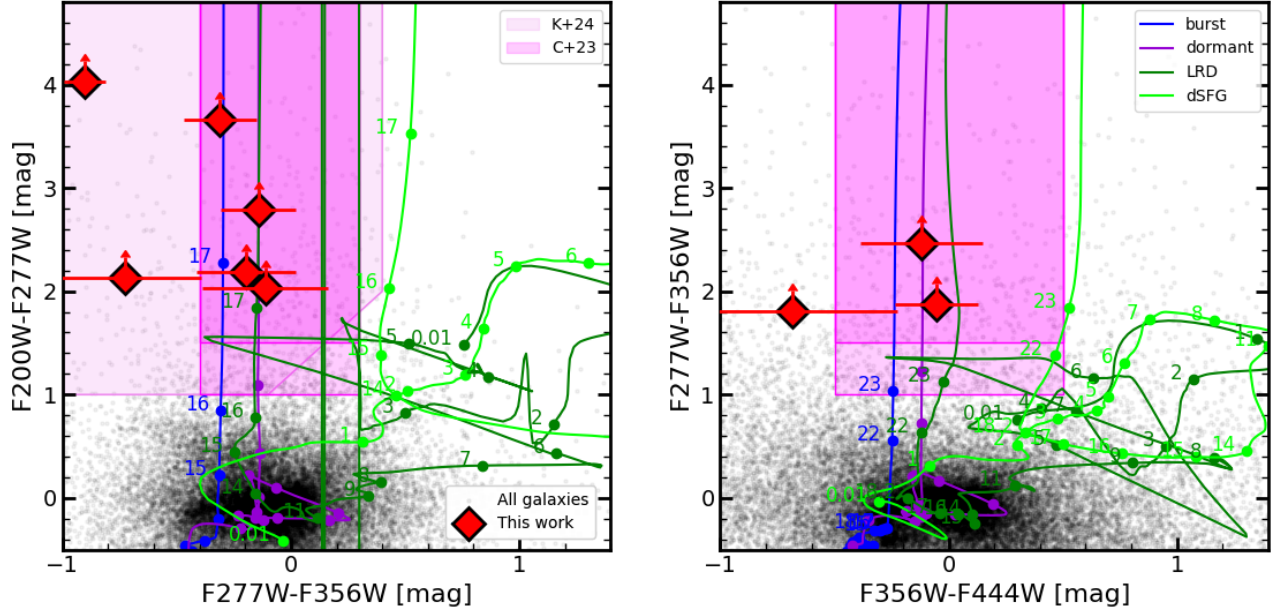
tral region. We further discuss UV slopes in Section 3.4. No interlopers of Galactic origin such as brown dwarfs are expected in our sample, since typically those sources have red F356W-F444W colors (see, e.g., Beiler et al. 2023 and Hainline et al. 2024b). We remark that there is a large number of sources (around 1500) whose colors are within the  $z > 16$  galaxy locus. Around 70% of them do not comply with the  $SNR > 5$  cut in the bands redward of the break. Out of the rest, half of the sources are located near bright objects or directly in star spikes that contaminate their photometry in one or several bands. All the rest have been rejected from our final sample based mainly on the photometric redshift quality and the visual vetting.

Figure 3 presents the SEDs and postage stamps of one of the  $z \sim 17$  and one of the  $z \sim 25$  galaxy candidates in our sample. Similar figures for the rest of the candidates are provided in Appendix A. The observational properties of our main sample are given in Table 2. In Appendix B, we provide a table with a few sources that lie on the edge of our identification limits for all selection criteria except one; they are dubious cases, and were not used in the calculations of the luminosity function presented in the following section.

### 3. RESULTS

#### 3.1. UV luminosity functions

To estimate luminosity functions, we calculate the absolute UV magnitudes ( $M_{UV}$ , averaged in a  $0.01 \mu\text{m}$  window around  $0.15 \mu\text{m}$ ) and their errors from SED fit-



**Figure 2.** Color-color diagrams characterizing the selection of F200W and F277W dropout galaxies. In each panel, our parent sample is shown with black dots. We remark that our sources have been selected by pre-identifying breaks, calculating photometric redshifts with prominent  $z > 10$  solutions, and visual vetting, i.e., our selection is not based directly on these color-color diagrams, but it is closely related to them. The  $z \sim 17$  and  $z \sim 25$  galaxy candidates are shown with red diamonds on the left and right panels, respectively. The color probing the Lyman break for these candidates (i.e., F200W-F277W and F277W-F356W) can only be measured as a lower limit (using  $1-\sigma$  detection thresholds for point-like sources), since we imposed a non-detection in the bluest band. In blue, we show the typical colors expected for a very young starburst as a function of redshift (representative values are marked with circles and labelled in the plots). In purple, we show the colors for a dormant galaxy, defined as a system that experienced a star-forming event 30 Myr ago. In light and dark green, we show the colors expected for typical interlopers in the selection of  $z \gtrsim 10$  galaxies, namely a little red dot template from Killi et al. (2023) and a dusty star-forming galaxy model from Pérez-González et al. (2023b). These redshift tracks show that  $z \gtrsim 16$  galaxies would present F200W-F277W colors redder than 1 mag and F277W-F356W colors bluer than 0.4 mag, a locus that has been proposed by authors such as Castellano et al. (2022, 2023, also in Castellano et al. 2025, in prep, private communication) and Kokorev et al. (2024) to select galaxies at these redshifts (regions shown in panels). The right panel shows similar behavior for  $z \gtrsim 23$  galaxies whose Lyman break is probed by the F277W-F356W color, while the F356W-F444W color probes the rest-frame UV spectral range.

ting, considering both the photometric and redshift uncertainties. No dust correction has been applied. The luminosity functions were constructed using the  $V_{\max}$  method (Efstathiou et al. 1988). Completeness was estimated by inserting artificial sources covering the magnitude range between 29 and 33 mag. We find that our catalog is 80% complete at  $F356W = 31.0$  mag, 50% at 31.4 mag, and 10% at 31.6 mag.

In addition to errors calculated with a Monte Carlo method using the absolute magnitude and photometric redshift uncertainties, we took into account cosmic variance effects by adding in quadrature values calculated by Ucci et al. (2021, see also Trenti & Stiavelli 2008; Bhowmick et al. 2020; Trapp & Furlanetto 2020). We estimate a 35–45% (30–40%) uncertainty in our lumi-

nosity function estimates at the bright (faint) ends due to field-to-field variations.

We show our luminosity functions at  $z \sim 17$  and  $z \sim 25$  in Figure 4. Our results are given in Table 3. We fit the data points with Schechter (1976) functions without any prior using an MCMC method. The results are given in Table 4.

Our estimate of the luminosity function is compared with others in the literature for the same absolute magnitude range  $-18 < M_{UV} < -19$  and similar redshifts from  $z \sim 14$  to  $z \sim 19$ . Our number densities are 0.1–0.5 dex smaller than direct estimates taken from those works. They are also consistent with the upper limits quoted by Morishita et al. (2024) and Whitley et al. (2025). Our calculations have also been compared with those obtained by Castellano et al. (2025, in prep, pri-



**Table 3.** Luminosity function data points.

$M_{UV}$	$\log \phi$	Volume	$M_{UV}$	$\log \phi$	Volume
[AB mag]	[ $\text{Mpc}^{-3} \text{ mag}^{-1}$ ]	[ $10^4 \text{ Mpc}^3$ ]	[AB mag]	[ $\text{Mpc}^{-3} \text{ mag}^{-1}$ ]	[ $10^4 \text{ Mpc}^3$ ]
	$z \sim 17$			$z \sim 25$	
-19.79	$< -4.8$	7.8	-18.99	$< -4.6$	5.5
-19.04	$-4.93^{+0.34}_{-1.38}$	7.8	-18.24	$-4.82^{+0.31}_{-0.75}$	4.7
-18.29	$-4.26^{+0.28}_{-0.63}$	3.1	-17.49	$-4.66^{+0.33}_{-1.11}$	1.8
-17.54	$-3.96^{+0.28}_{-0.58}$	1.3			

**Table 4.** Luminosity function parameters.

Parameter	$z \sim 17$	$z \sim 25$
$\alpha$	$-2.12^{+0.15}_{-0.09}$	$-2.12^{+0.13}_{-0.22}$
$M^*$ [AB mag]	$-19.0^{+1.0}_{-0.5}$	$-18.5^{+0.8}_{-0.4}$
$\phi^*$ [ $10^{-5} \text{ Mpc}^{-3} \text{ mag}^{-1}$ ]	$3.55^{+0.49}_{-0.15}$	$1.22^{+0.58}_{-0.28}$
$\log \rho_{UV}$ [ $10^{24} \text{ erg s}^{-1} \text{ Hz}^{-1} \text{ Mpc}^{-3}$ ]	$0.89^{+0.45}_{-0.49}$	$0.13^{+0.14}_{-0.08}$

NOTE—Results for the [Schechter \(1976\)](#) parametrization fits to the luminosity functions at  $z \sim 17$  and  $z \sim 24$  presented in Fig. 4. The last row shows the integrated luminosity for absolute magnitudes  $M_{UV} < -17$  mag.

vate communication) for the same absolute magnitude range. The number densities estimated in our work are consistent with their upper limits, obtained by analyzing a number of deep fields adding up an area nearly 40 times larger than ours, but characterized by shallower depths.

Comparing with luminosity functions estimated at  $z = 9 - 12$ , exemplified in Figure 4 with those presented by [Pérez-González et al. 2023a](#), we find a  $\times 4$  number density evolution from  $z \sim 17$  to  $z \sim 12$  (corresponding to a 150 Myr Universe age difference), and  $\times 8$  from  $z \sim 25$  to  $\sim 17$  (in 80 Myr), implying rapid build-up of stars starting some time after the first 100 Myr of cosmic time. The dispersion in the luminosity function estimates at  $z \sim 12$  is 0.2 dex (see [Donnan et al. 2024](#) for a recent compilation), so the factors quoted above for our luminosity function evolution have relative errors of  $\sim 50\%$ . The dispersion in estimates at  $z \sim 17$  in the absolute magnitude range covered by our survey is larger, 0.4 dex, with some works obtaining much smaller evolution from  $z \sim 12$  to  $z \sim 17$ .

### 3.2. Cosmic UV luminosity density evolution

Figure 5 presents the cosmic UV luminosity density obtained from integrating the luminosity functions shown in Figure 4 down to the same absolute magnitude, i.e., for  $M_{UV} \sim -17$  mag. The density (in logarithmic scale) evolves roughly linearly with respect to redshift

from  $z \sim 10$  to  $z \sim 25$ , decreasing by a factor of  $\sim 2.5$  in the 100 Myr from  $z \sim 10$  to  $z \sim 14$  based on values from the literature, and, taking into account the results in this work, it continues decreasing faster, by a factor of  $\sim 3$  in the previous 100 Myr ( $z \sim 14$  to  $z \sim 18$ ), and another factor of  $\sim 3$  in the previous  $\sim 80$  Myr (back to  $z \sim 25$ ).

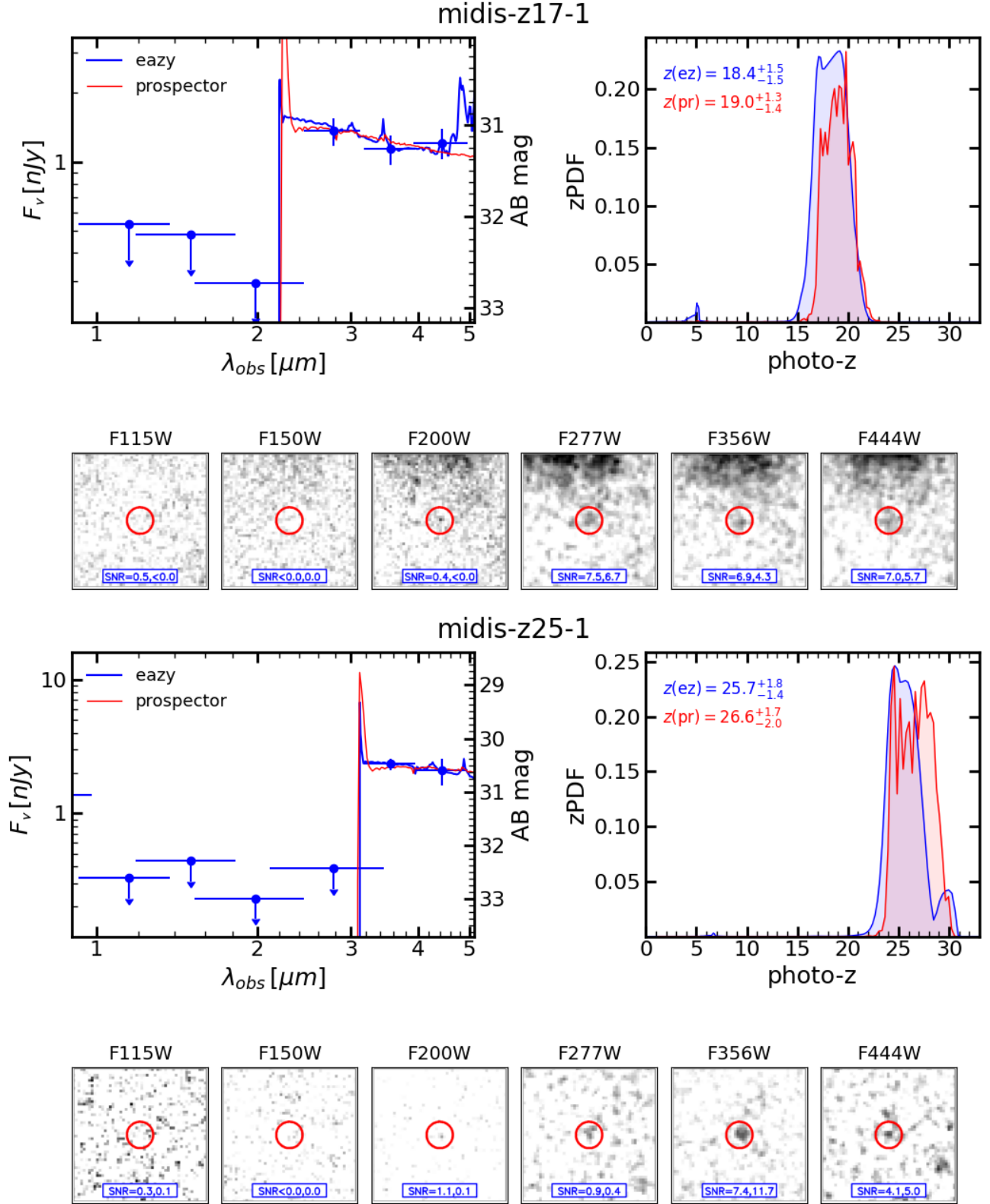
Using the UV luminosity density data points at  $z = 9, 11, 12$  from [Pérez-González et al. \(2023a\)](#) and the results at  $z \sim 17$  and  $z \sim 25$  from this work, we fit the redshift dependence of the evolution of the UV luminosity density in the  $10 < z < 25$  interval, obtaining that it evolves as:

$$\rho_{UV} \propto (1+z)^{-5.3 \pm 1.6}. \quad (1)$$

### 3.3. Comparison with cosmological galaxy formation models

Figures 6 and 7 show comparisons of the evolution at  $z > 10$  of the observationally derived luminosity function and UV luminosity density with several recent galaxy evolution models. These include an updated version of the Santa Cruz Semi-Analytic Model ([Somerville et al. 2008; Yung et al. 2024a](#)), presented by Somerville et al. (in prep; hereafter S25), as well as the models of [Dekel et al. \(2023\)](#) and [Ferrara et al. \(2023\)](#).

The updated Santa Cruz SAMs shown here are based on results from molecular cloud-scale simulations with



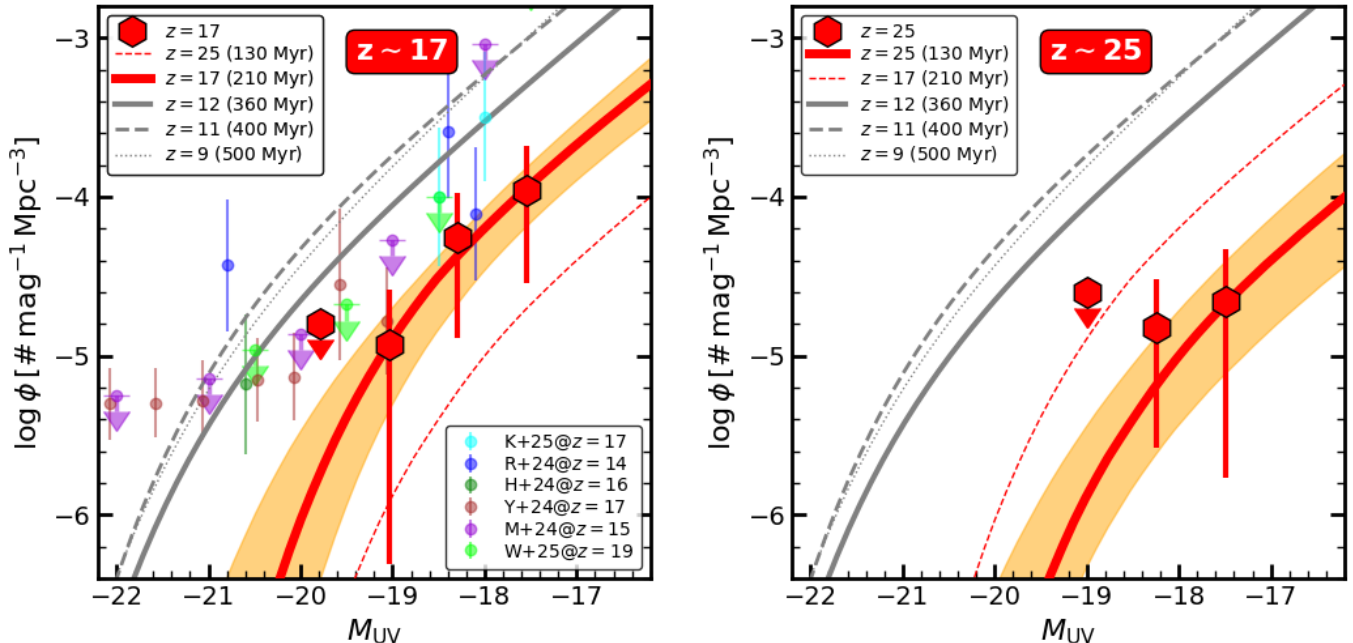


**Figure 4.** Luminosity functions at  $z \sim 17$  (left panel) and  $z \sim 25$  (right panel) estimated in this paper (red diamonds) and Schechter (1976) fits (red line and  $1 - \sigma$  uncertainties in orange). On the left, symbols show literature estimates from Harikane et al. (2024, green), Robertson et al. (2024, blue), Yan et al. (2023b, brown), Kokorev et al. (2024, cyan), Morishita et al. (2024, violet), and Whittler et al. (2025, lime). The panels also show in gray the Schechter fits to the luminosity functions presented in Pérez-González et al. (2023a) for  $z = 9, 11, 12$  (dashed, dotted, and continuous line, respectively), as well as the results from this paper for the other redshift bin (red dashed line, for  $z \sim 25$  on the left panel, for  $z \sim 17$  on the right one). The age of the Universe for the redshifts of all these luminosity functions are given in the legend.

radiative transfer by Menon et al. (2024), which indicate that higher surface density clouds have higher star formation efficiencies, converting up to 85% of their available gas into stars within a cloud lifetime, in contrast to a few percent in lower density, local Universe molecular clouds. The S25 models assume that the surface density of clouds is proportional to the average surface density of the overall ISM in galaxies. Because the ISM is expected to be denser at higher redshift, these models predict higher star formation efficiencies at early times. The main uncertain parameter in these models is the fraction of the ISM in dense star forming clouds, which is represented by the parameter  $f_{\text{dense}}$ .

In the "feedback free starburst" (FFB) model of Dekel et al. (2023, see also Li et al. 2024), it is posited that when the galaxy free-fall time is shorter than the timescale for the first supernovae to begin to explode (a few Myr), star formation is more efficient because of the absence of strong supernovae driven winds. These conditions become more common in the most massive halos above  $z \sim 10$  (Dekel et al. 2023), again because of the higher expected density of the ISM. These models

are also parameterized by the unknown efficiency of star formation (here denoted as  $\epsilon_{\text{FFB}}$ ).

In the Ferrara et al. (2023, hereafter F23) model, the shallower than expected evolution of the luminosity function and luminosity density at  $z \gtrsim 10$  is explained as being due to ejection of dust via radiation pressure above a critical specific star formation rate, which again is expected to be more frequently attained in higher redshift galaxies.

First considering the UV luminosity function comparison, the F23 model reproduces the observations at  $z \sim 10-12$ , but underproduces the galaxy number density at higher redshifts. The FFB models reproduce the observations at  $z \sim 10-12$  well for the lower values of SFE  $\epsilon_{\text{FFB}} = 0.3$ , but require higher values  $\epsilon_{\text{FFB}} \sim 1$  (above 0.5 if we consider uncertainties in the LF at  $z \sim 17$  presented in this paper) to reproduce the UVLF at  $z \sim 14-17$ . Even the  $\epsilon_{\text{FFB}} \sim 1$  FFB model lies below the observational estimate at  $z \sim 25$ . The S25 Santa Cruz SAM with density modulated star formation efficiency, similarly, matches the lower redshift UV luminosity functions well with the lower values of the dense gas fraction ( $f_{\text{dense}} = 0.1$ ), but higher values of  $f_{\text{dense}}$ ,

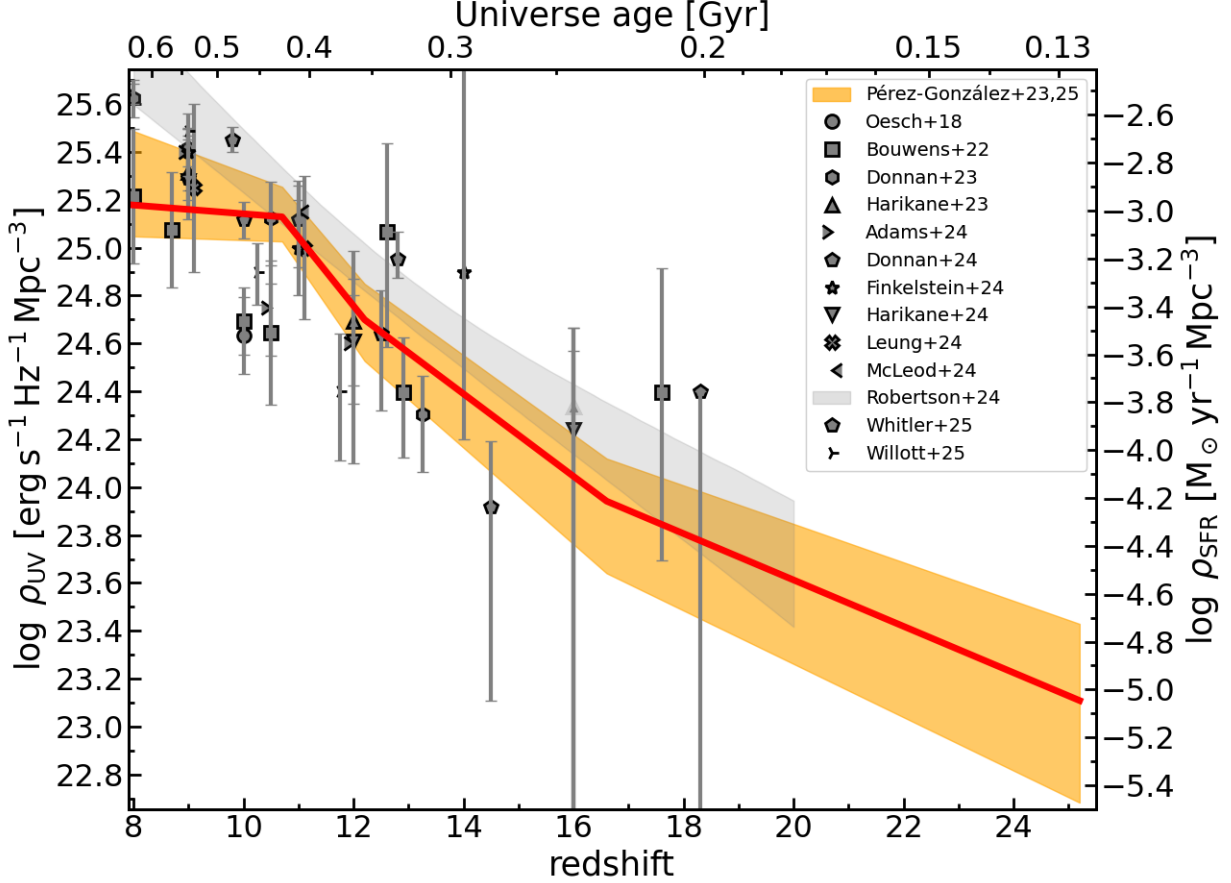


**Figure 5.** Evolution with redshift (age of the Universe given on top axis) of the UV luminosity density, transformed into SFR density on the right vertical axis (assuming a [Chabrier 2003](#) IMF). Our results are plotted with a red line joining the most probable values and orange shaded region for  $1 - \sigma$  errors. Estimates from the literature are plotted with gray symbols ([Oesch et al. 2018](#); [Bouwens et al. 2022a,b](#); [Donnan et al. 2023, 2024](#); [Harikane et al. 2023](#); [Adams et al. 2024](#); [Finkelstein et al. 2024](#); [Harikane et al. 2024](#); [Leung et al. 2023](#); [McLeod et al. 2024](#); [Robertson et al. 2024](#); [Whitler et al. 2025](#); [Willott et al. 2024](#)).

approaching unity and at least around  $f_{\text{dense}} = 0.5$ , appear to be required to reproduce the observed UV LF at  $z \sim 17$ . Predictions above  $z \sim 20$  for this model are not currently available.

The integrated UV luminosity density tells a similar story. None of the theoretical models predicts as shallow a decline in  $\rho_{UV}$  from  $z \sim 12$ – $17$  as that implied by our observations. The discrepancy between the predicted very steep drop in  $\rho_{UV}$  from  $z \sim 17$ – $24$  with our results is even more dramatic. The  $\log \rho_{UV}$  evolution for models follows a  $(1+z)^\gamma$  law with  $\gamma \sim -6$  at  $10 \lesssim z \lesssim 12$ , very similar to observations, but that exponent is closer to  $\gamma \sim -4$  at  $z > 12$ . If we assume that the halo mass functions derived from the  $\Lambda$ CDM model are correct, then this means that the amount of (UV) light created in the halos considered in the simulations is significantly smaller than what is observed and that evolves with redshift.

We note that the halo mass function at  $z \gtrsim 20$  has not been well-characterized with modern N-body simulations with up-to-date cosmological parameters. The predictions of [Dekel et al. \(2023\)](#), shown here, adopt an extrapolation of a fit to a halo mass function based on N-body simulations analyzed at much lower redshifts and over a very different halo mass range. The semi-analytic models of S25 are based on halo merger trees extracted from the N-body simulations presented by [Yung et al. \(2024b\)](#), but due to resolution limitations of those simulations, the merger trees do not extend beyond  $z \sim 20$ . The predictions at the highest redshifts shown here should therefore be taken with some caution.

To further understand the implications of our observed luminosity functions, and assuming that the  $\Lambda$ CDM cosmology holds, we calculate the mass-to-light ratios needed to reproduce these current observations. For this calculation, we start with the dark matter halo

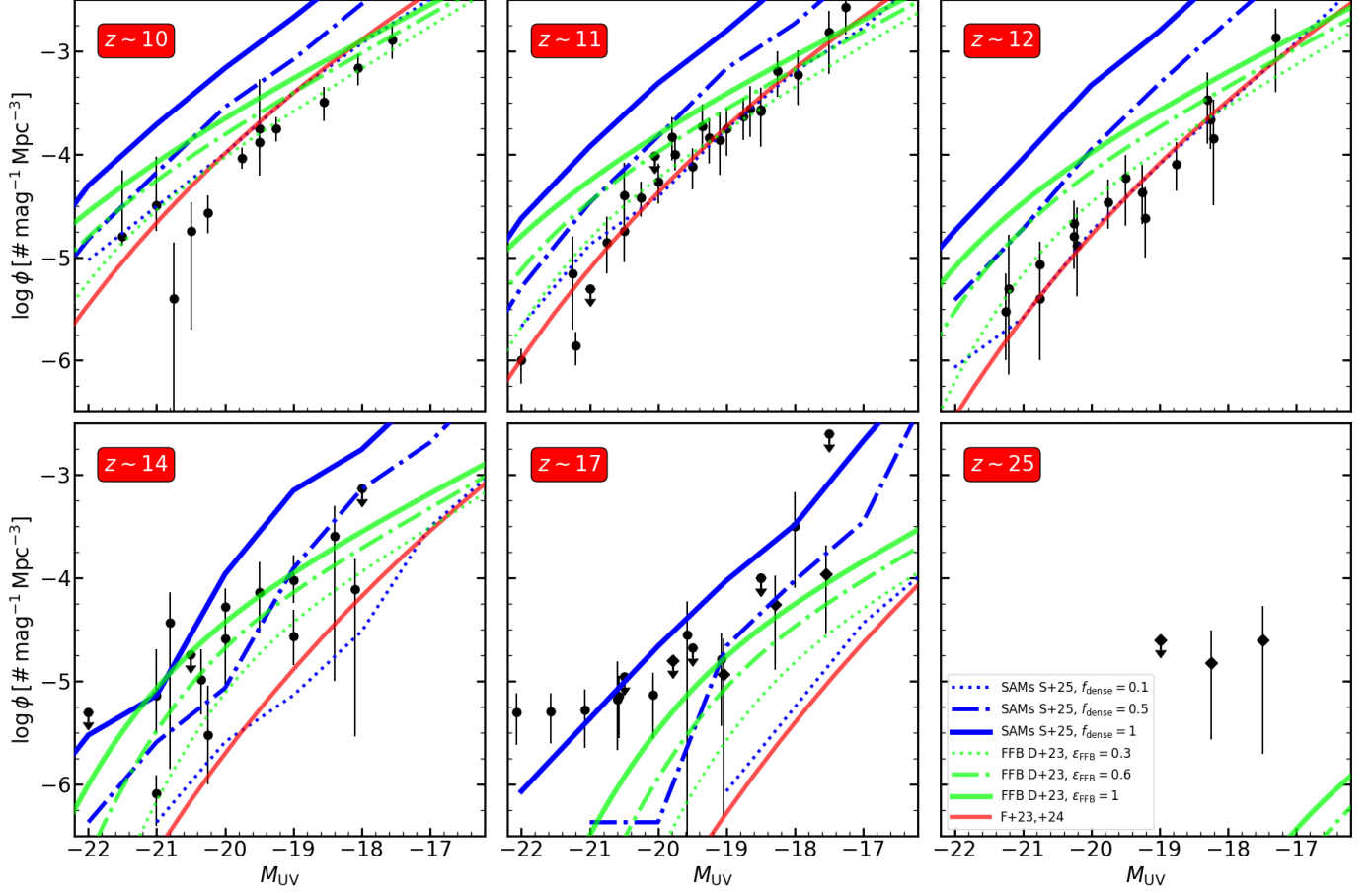


**Figure 6.** Comparison of the observations and model predictions for the evolution of the UV luminosity function at  $z > 10$ . The literature compilation includes the results in this paper as well as those in Adams et al. (2024); Bouwens et al. (2022a); Casey et al. (2024); Castellano et al. (2023); Donnan et al. (2023, 2024); Finkelstein et al. (2022, 2024); Harikane et al. (2022, 2024); Kokorev et al. (2024); Leung et al. (2023); Morishita et al. (2024); Naidu et al. (2022); Robertson et al. (2024); Whittler et al. (2025); Willott et al. (2024); Yan et al. (2023b). The models are: (1) the feedback-free burst models in Dekel et al. (2023, FFB, see also Li et al. 2024), including several star formation efficiencies,  $\epsilon_{\text{FFB}} = 0.3, 0.6, 1.0$ , and for their disc dust recipe (lime color); (2) the models including the effects and blowout of dust from Ferrara et al. (2023, see also Ferrara 2024; red); and (3) the semi-analytic models with density-dependent star formation efficiency, with dense gas fraction  $f_{\text{dense}} = 0.1, 0.5, 1$ , from Somerville et al. (in prep), only up to  $z \sim 17$ , as no predictions are available at  $z \gtrsim 20$  (blue).

mass functions obtained by Yung et al. (2024b)<sup>1</sup>. Then, we calculate the ratio for a given number density to convert that mass function to the luminosity functions estimated for  $z \sim 9$  to  $z \sim 25$  by Pérez-González et al. (2023a) and this paper. This operation is analogous to the abundance matching technique used to compare stellar and dark matter mass functions (e.g., Behroozi et al. 2010; Trujillo-Gomez et al. 2011). However, we remark that we rank halos according to dark matter halo mass and UV luminosity, and not stellar mass directly. The stellar mass calculations include larger un-

certainties than the directly observed luminosities, but the caveat is that bursts can make a galaxy jump to a higher luminosity state than the average it would get for its halo abundance. The final result is a mass-to-light ratio (M/L) that depends on the mass of the halo and redshift. The M/L obtained with this method refers to dark matter halo masses. We translate these into baryon mass by multiplying by the relative baryon abundance with respect to dark matter, and then we apply a star formation efficiency  $\epsilon$ , i.e., the fraction of mass transformed to stars relative to the total amount of baryons in the halo.

Figure 8 shows our results for the derived mass-to-light ratios for  $\epsilon = 0.15$  (similar to the values adopted by Lei et al. 2025; Harikane et al. 2022). We compare the mass-to-light ratios with those obtained from a com-

<sup>1</sup> Similar results were obtained when using the functions provided by the HMF code for Tinker et al. (2008) halos, extended to high redshift by Behroozi et al. (2013)

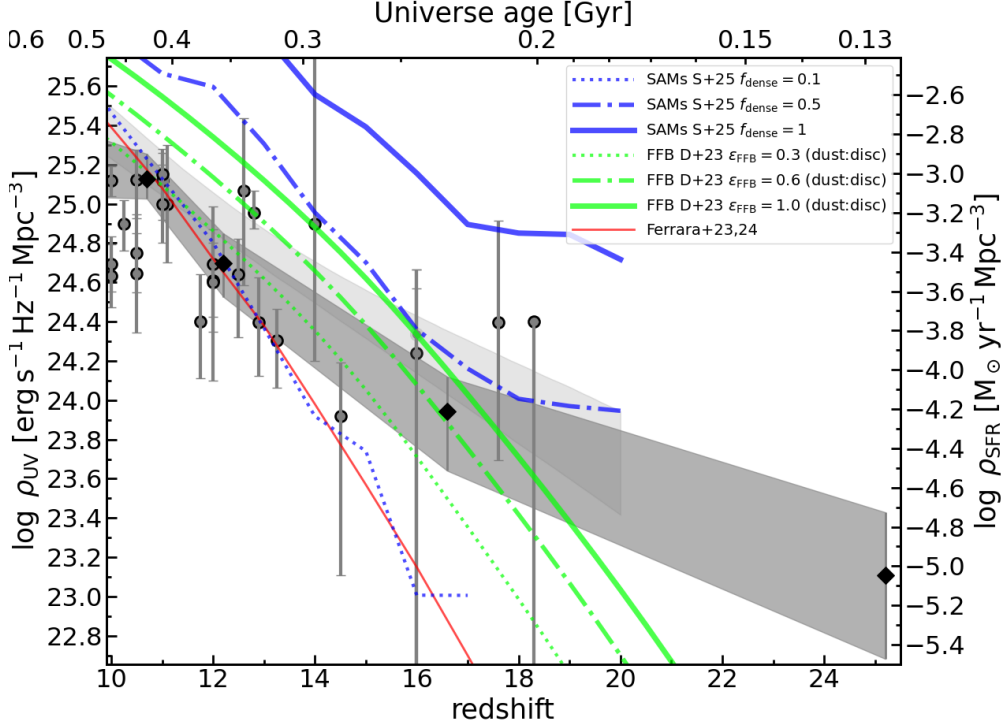


**Figure 7.** Comparison of the observations and model predictions for the evolution of the UV luminosity density at  $z > 10$ . Results from this paper and the literature (see Figure 5 for references) are compared with predictions from the same models depicted in Figure 6.

prehensive list of stellar population models for different stellar ages (typical of  $z > 10$  galaxies; see, for example, Carniani et al. 2024; Helton et al. 2024; Robertson et al. 2023) spanning the whole range of expected metallicities as well as a variety of possible IMFs (Zackrisson et al. 2011).

Figure 8 shows that, based on this abundance matching exercise, the typical host halo mass for the faintest galaxies that are currently observable by JWST shifts from  $10^{11} M_{\odot}$  at  $z \sim 9$  down to  $\sim 10^{9.4} M_{\odot}$  at  $z \sim 17$  and even further down to  $\sim 10^{8.4} M_{\odot}$  at  $z \sim 25$ . In particular, the intrinsic UV magnitude of the populations we detect at  $z \sim 17$  and  $z \sim 25$  are similar ( $-17 < M_{UV} < -18$ ), yet the host halo mass required to match the detected abundance is an order of magnitude smaller. Leaving aside the possibility of non-stellar contributions to the UV luminosity, this implies that either halos are more efficient at converting baryons into stars, or that stellar populations are brighter for a given amount of stars formed.

Now to investigate how this compares with the expected stellar mass-to-light ratios from stellar population models, in Figure 8 we also show  $M_{\star}/L_{UV}$  from a variety of stellar population models with a mean age of 1 Myr or 30 Myr (Zavala et al. 2025) and low ( $< 0.1\% Z_{\odot}$ ) to primordial metallicities. We can see that the results

for a 30 Myr old stellar population are consistent with the required  $M_{\star}/L_{UV}$  at  $z = 17$  for our adopted (constant) value of  $\epsilon = 0.15$ . The factor of approximately three lower values of  $M_{\star}/L_{UV}$  at  $z \sim 25$  imply that these  $z \sim 25$  galaxies, if the  $\epsilon$  is constant (15% assumed in the plot), should host much younger stellar populations (i.e., catching the galaxies in a very young burst), and/or a top-heavy IMF. Alternatively, if  $z \sim 25$  the star formation efficiency changes but the typical stellar properties at  $z \sim 17$  and  $z \sim 25$  are similar, the relative efficiency between these two epochs (and halos of different masses) must change. For example, if the efficiency at  $z \sim 17$  stays at 15%, the  $z \sim 25$  galaxies must present higher values to go up in the plot to the same  $M_{\star}/L_{UV}$  values; or if the  $z \sim 25$  galaxies remain in the  $\epsilon = 0.15$  efficiency and mass-to-light ratios typical of young low-metallicity starburst,  $z \sim 17$  galaxies should have smaller star formation efficiencies to match those stellar ages. Given that the probability of catching a galaxy in a 1 Myr old starburst should be smaller than catching it with older ages, the first example seems more representative. However, the detectability of the highest redshift galaxies might bias the selection to the youngest and brightest evolutionary stages, which, would favor the second scenario.

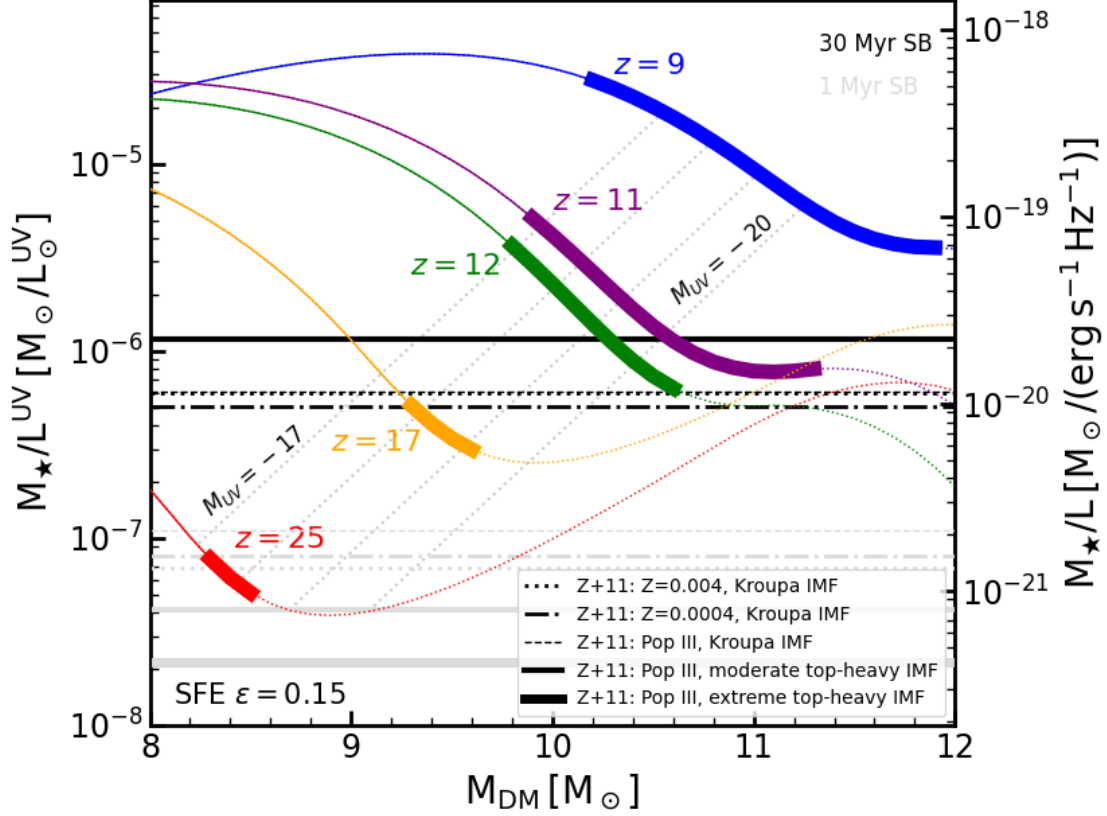


**Figure 8.** Stellar mass-to-light ratios as a function of halo mass for redshifts  $z \sim 9$  to  $z \sim 25$ . The left y-axis give UV luminosity densities in solar units (assuming an AB absolute magnitude for the Sun  $M_{\odot}^{UV} = 17.30$ , Willmer 2018), the right y-axis in CGS units. The vertical axes could also be read in terms of dark matter mass-to-light ratios considering the baryon-to-dark matter density ratio ( $\sim 19\%$ ) and the star formation efficiency, defined as stellar mass divided by baryon mass, assumed to be 15% in the plot. The curved lines provide results based on an abundance matching comparison between luminosity functions from this work and Pérez-González et al. (2023a) and dark matter mass functions from Yung et al. (2024b). Thick segments show the calculations based on the range of absolute magnitudes actually probed by those works, while the thin lines show results based on extrapolated Schechter fits. We differentiate between the faint/light ends of the luminosity and mass functions, which might be well characterized by the current data with a faint-end slope (where we use a continuous line) and the bright/massive ends, whose behavior is more complex and unconstrained for most redshifts above  $z = 10$  (where we used a dotted line). Oblique lines show the UV absolute magnitudes corresponding to the dark matter masses according to the abundance matching exercise, running from -17 to -20 every one magnitude (the extreme values are marked). Horizontal lines show mass-to-light ratios for a compilation of relevant stellar populations models from Zackrisson et al. (2011), with metallicities spanning expected values from  $1/5 Z_{\odot}$  to Pop-III stars, and different IMFs including Kroupa (2001) and top-heavy parametrizations. Lines in black and light gray show predictions for 30 and 1 Myr old instantaneous bursts. We note that the models with the most extreme top-heavy IMF do not extend to 30 Myr, those massive stars die earlier. This effect also affects the relative mass-to-light ratios between the Kroupa and top-heavy IMFs for 30 Myr (reversed compared to 1 Myr predictions).

Directly related to the previous point, we remark that Figure 8 is constructed with an abundance matching method applied to dark matter mass functions and UV luminosity functions. Bursty star formation histories might enhance the UV photon production of halos with smaller masses than those corresponding to the same number density of the luminosity function. The small number of galaxies in the sample discussed in this paper

would worsen these effects, as we might be biased preferentially towards galaxies that are experiencing a very recent or ongoing burst.

#### 3.4. Stellar populations of $z \sim 17$ and $z \sim 25$ galaxy candidates

**Table 5.** Physical properties of the galaxy candidates at  $14 < z < 25$ .

Galaxy name	code	redshift	$\beta$	log $M_{\star}$	A(V)	$t_{m-w}$	< SFR >
				[ $M_{\odot}$ ]	[mag]	[Myr]	[ $M_{\odot}/\text{yr}$ ]
$z \sim 17$ sample							
midis-z17-1	sy-BC03	$18.4^{+1.5}_{-1.5}$	$-2.7^{+0.6}_{-0.2}$	$7.5^{+0.5}_{-0.5}$	$0.00^{+0.21}_{-0.00}$	$24 \pm 1$	$1.1 \pm 0.5$
	sy-Z11	$18.4^{+1.5}_{-1.5}$	$-3.0^{+0.4}_{-0.1}$	$7.3^{+0.6}_{-0.4}$	$0.00^{+0.19}_{-0.00}$	$13 \pm 4$	$1.0 \pm 0.4$
	sy-BPASS	$18.4^{+1.5}_{-1.5}$	$-2.6^{+0.4}_{-0.3}$	$5.9^{+0.4}_{-0.1}$	$0.00^{+0.10}_{-0.00}$	$1 \pm 1$	$0.4 \pm 0.1$
	pr-FSPS	$19.0^{+1.2}_{-1.4}$	$-2.3^{+0.1}_{-0.1}$	$7.4^{+7.6}_{-7.1}$	$0.27^{+0.46}_{-0.10}$	$154 \pm 62$	$0.1 \pm 0.1$
midis-z17-2	sy-BC03	$17.4^{+1.4}_{-1.1}$	$-3.0^{+0.6}_{-0.1}$	$6.5^{+0.6}_{-0.1}$	$0.00^{+0.10}_{-0.00}$	$3 \pm 1$	$0.6 \pm 0.1$
	sy-Z11	$17.4^{+1.4}_{-1.1}$	$-3.0^{+0.7}_{-0.1}$	$6.6^{+0.8}_{-0.1}$	$0.00^{+0.10}_{-0.00}$	$1 \pm 1$	$4.2 \pm 0.8$
	sy-BPASS	$17.4^{+1.4}_{-1.1}$	$-2.9^{+0.3}_{-0.2}$	$5.9^{+0.4}_{-0.1}$	$0.00^{+0.10}_{-0.00}$	$1 \pm 1$	$0.4 \pm 0.1$
	pr-FSPS	$18.9^{+0.8}_{-1.9}$	$-2.1^{+0.1}_{-0.1}$	$7.2^{+7.4}_{-6.9}$	$0.19^{+0.39}_{-0.07}$	$132 \pm 56$	$0.1 \pm 0.1$
midis-z17-3	sy-BC03	$17.3^{+1.1}_{-0.2}$	$-3.0^{+0.2}_{-0.1}$	$7.3^{+0.2}_{-0.2}$	$0.00^{+0.10}_{-0.00}$	$2 \pm 1$	$6.8 \pm 1.2$
	sy-Z11	$17.3^{+1.1}_{-0.2}$	$-3.0^{+0.2}_{-0.1}$	$7.3^{+0.2}_{-0.2}$	$0.00^{+0.10}_{-0.00}$	$1 \pm 1$	$6.8 \pm 1.3$
	sy-BPASS	$17.3^{+1.1}_{-0.2}$	$-3.0^{+0.2}_{-0.1}$	$5.6^{+0.2}_{-0.2}$	$0.00^{+0.10}_{-0.00}$	$1 \pm 1$	$0.2 \pm 0.0$
	pr-FSPS	$19.1^{+0.1}_{-0.1}$	$-2.2^{+0.1}_{-0.1}$	$6.7^{+6.8}_{-6.7}$	$0.01^{+0.10}_{-0.00}$	$4 \pm 2$	$0.6 \pm 0.6$
midis-z17-4	sy-BC03	$18.0^{+1.7}_{-1.5}$	$-2.6^{+0.2}_{-0.4}$	$7.7^{+0.6}_{-0.3}$	$0.11^{+0.24}_{-0.01}$	$25 \pm 1$	$1.6 \pm 0.8$
	sy-Z11	$18.0^{+1.7}_{-1.5}$	$-2.7^{+0.2}_{-0.1}$	$7.0^{+0.8}_{-0.2}$	$0.03^{+0.16}_{-0.02}$	$42 \pm 1$	$1.4 \pm 0.5$
	sy-BPASS	$18.0^{+1.7}_{-1.5}$	$-2.5^{+0.4}_{-0.3}$	$6.8^{+0.6}_{-0.1}$	$0.10^{+0.10}_{-0.01}$	$43 \pm 1$	$4.7 \pm 0.9$
	pr-FSPS	$19.1^{+0.5}_{-0.5}$	$-1.1^{+0.1}_{-0.1}$	$7.6^{+7.8}_{-7.3}$	$0.45^{+0.60}_{-0.27}$	$113 \pm 64$	$0.2 \pm 0.2$
midis-z17-5	sy-BC03	$17.5^{+2.3}_{-2.4}$	$-2.8^{+0.6}_{-0.6}$	$6.7^{+0.6}_{-0.5}$	$0.00^{+0.10}_{-0.00}$	$20 \pm 1$	$1.7 \pm 0.6$
	sy-Z11	$17.5^{+2.3}_{-2.4}$	$-3.0^{+0.8}_{-0.1}$	$7.2^{+0.6}_{-0.3}$	$0.00^{+0.23}_{-0.00}$	$12 \pm 2$	$1.2 \pm 0.4$
	sy-BPASS	$17.5^{+2.3}_{-2.4}$	$-2.5^{+0.4}_{-0.3}$	$6.2^{+0.3}_{-0.1}$	$0.00^{+0.10}_{-0.00}$	$1 \pm 1$	$1.3 \pm 0.2$
	pr-FSPS	$18.3^{+2.1}_{-2.5}$	$-2.2^{+0.1}_{-0.1}$	$7.4^{+7.6}_{-7.1}$	$0.33^{+0.57}_{-0.13}$	$120 \pm 44$	$0.1 \pm 0.1$
midis-z17-6	sy-BC03	$16.8^{+2.4}_{-0.8}$	$-2.4^{+0.2}_{-0.2}$	$8.3^{+0.2}_{-0.2}$	$0.01^{+0.17}_{-0.01}$	$59 \pm 1$	$3.3 \pm 0.8$
	sy-Z11	$16.8^{+2.4}_{-0.8}$	$-2.6^{+0.4}_{-0.3}$	$8.2^{+0.2}_{-0.7}$	$0.00^{+0.20}_{-0.00}$	$36 \pm 4$	$3.8 \pm 0.9$
	sy-BPASS	$16.8^{+2.4}_{-0.8}$	$-2.7^{+0.1}_{-0.1}$	$6.8^{+0.1}_{-0.1}$	$0.00^{+0.10}_{-0.00}$	$1 \pm 1$	$4.7 \pm 0.9$
	pr-FSPS	$16.5^{+2.1}_{-0.9}$	$-2.2^{+0.1}_{-0.1}$	$7.7^{+7.9}_{-7.5}$	$0.22^{+0.37}_{-0.10}$	$165 \pm 56$	$0.2 \pm 0.2$
midis-z25-1	sy-BC03	$25.7^{+1.8}_{-1.4}$	$-2.6^{+0.6}_{-0.2}$	$7.1^{+0.6}_{-0.5}$	$0.19^{+0.10}_{-0.01}$	$14 \pm 1$	$4.1 \pm 0.8$
	sy-Z11	$25.7^{+1.8}_{-1.4}$	$-2.7^{+0.6}_{-0.1}$	$7.1^{+1.5}_{-0.1}$	$0.10^{+0.10}_{-0.01}$	$31 \pm 1$	$13.7 \pm 2.8$
	sy-BPASS	$25.7^{+1.8}_{-1.4}$	$-2.6^{+0.6}_{-0.5}$	$5.6^{+0.4}_{-0.2}$	$0.11^{+0.10}_{-0.01}$	$9 \pm 1$	$0.2 \pm 0.0$
	pr-FSPS	$26.6^{+1.7}_{-2.0}$	$-2.0^{+0.1}_{-0.1}$	$7.5^{+7.7}_{-7.2}$	$0.33^{+0.55}_{-0.13}$	$90 \pm 38$	$0.2 \pm 0.2$
midis-z25-2	sy-BC03	$25.1^{+1.5}_{-1.0}$	$-3.0^{+0.7}_{-0.1}$	$6.8^{+0.1}_{-0.1}$	$0.00^{+0.10}_{-0.00}$	$2 \pm 1$	$2.0 \pm 0.4$
	sy-Z11	$25.1^{+1.5}_{-1.0}$	$-3.0^{+0.1}_{-0.1}$	$6.9^{+0.1}_{-0.1}$	$0.00^{+0.10}_{-0.00}$	$1 \pm 1$	$7.1 \pm 1.3$
	sy-BPASS	$25.1^{+1.5}_{-1.0}$	$-3.0^{+0.1}_{-0.1}$	$6.5^{+0.1}_{-0.1}$	$0.00^{+0.10}_{-0.00}$	$1 \pm 1$	$2.4 \pm 0.7$
	pr-FSPS	$24.9^{+2.3}_{-1.5}$	$-2.1^{+0.1}_{-0.1}$	$7.2^{+7.5}_{-7.0}$	$0.29^{+0.52}_{-0.10}$	$89 \pm 36$	$0.1 \pm 0.1$
midis-z25-3	sy-BC03	$25.6^{+1.5}_{-1.6}$	$-2.4^{+0.8}_{-0.4}$	$7.9^{+0.6}_{-0.6}$	$0.07^{+0.23}_{-0.07}$	$37 \pm 1$	$2.7 \pm 0.7$
	sy-Z11	$25.6^{+1.5}_{-1.6}$	$-2.7^{+0.6}_{-0.1}$	$7.4^{+0.8}_{-0.5}$	$0.07^{+0.24}_{-0.07}$	$32 \pm 14$	$3.0 \pm 1.1$
	sy-BPASS	$25.6^{+1.5}_{-1.6}$	$-2.4^{+0.3}_{-0.4}$	$6.3^{+0.7}_{-0.3}$	$0.14^{+0.10}_{-0.01}$	$58 \pm 1$	$2.4 \pm 0.7$
	pr-FSPS	$26.6^{+1.6}_{-1.3}$	$-2.3^{+0.1}_{-0.1}$	$7.4^{+7.7}_{-7.2}$	$0.32^{+0.55}_{-0.13}$	$76 \pm 33$	$0.2 \pm 0.2$

NOTE—Physical properties of the sample of  $z > 14$  galaxy candidates presented in this paper. We provide: (1) photometric redshift, more specifically, the most probable according to the integral of the zPDF, including errors (**eazy** value for SYNTHESIZER-AGN, free parameter in **prospector**); (2) UV slope measured from SED-fitting; (3) stellar masses, attenuations, mass-weighted ages, and average SFRs, provided by the SED modeling using SYNTHESIZER-AGN (with three different stellar emission libraries: BC03, Z11, and BPASS), and **prospector** (using the FSPS library).

We estimated stellar masses for our  $z > 16$  galaxy candidates using **prospector** (see Section 2) as well as the SYNTHESIZER-AGN code (Pérez-González et al. 2003, 2008). For the latter, we used three different stellar emission libraries, namely, Bruzual & Charlot (2003, BC03 hereafter), Zackrisson et al. (2011, Z11), and Eldridge et al. (2017, BPASS). In all cases, we only considered models with metallicities lower than  $0.2 Z_{\odot}$ , expected and observed at these redshifts (e.g.,

Curti et al. 2023; Nakajima et al. 2023; Sanders et al. 2024). As for the IMF, we used Chabrier (2003) for BC03 and BPASS, and Kroupa (2001) for Z11. We assumed delayed-exponentials to model the star formation history, with timescales ranging from 1 Myr to 1 Gyr. Dust was considered using the Calzetti et al. (2000) attenuation law (differently affecting the stellar and gas emission, with a constant factor in this modeling) and assuming  $V$ -band attenuations smaller than 1 mag. The



redshift was fixed to the most probable value provided by **eazy**. Jointly with stellar masses, we also estimated UV spectral slopes  $\beta$  for each code. Uncertainties in all the SED fitting results were calculated using a Monte Carlo method by varying the flux data points according to their photometric errors and refitting. Results for each galaxy are given in Table 5.

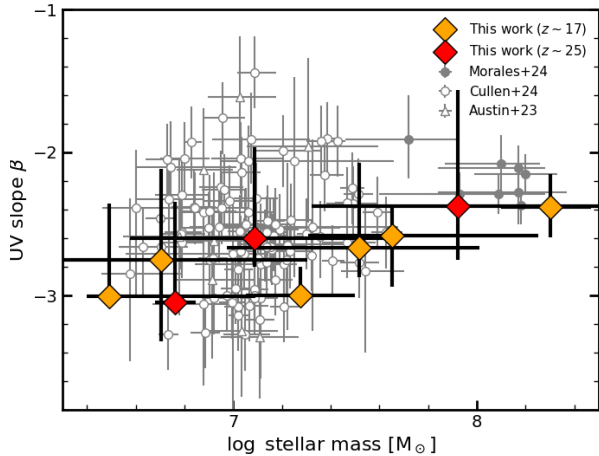


**Figure 9.** UV spectral slope  $\beta$  (obtained from SED fitting, with errors accounting for photometric uncertainties; for the plot, we use the estimations based on SYNTHESIZER-AGN and BC03 models) *vs.* stellar mass. The results for the  $z \sim 17$  and  $z \sim 25$  samples presented in this work are compared with values for  $z > 10$  galaxies in the compilations discussed in Cullen et al. (2023), Austin et al. (2024), and Morales et al. (2024).

Figure 9 shows our  $z > 16$  galaxy candidates in a  $\beta$  *vs.*  $M_{\star}$  plot, compared to other lower redshift samples in the literature including  $z > 10$  galaxies (and typically  $z < 12$ ). For this plot, we use the estimates based on SYNTHESIZER-AGN and BC03 models.

Typical stellar masses (median and quartiles) for our sample are  $\log M_{\star}/M_{\odot} = 7.4_{6.8}^{7.9}$ , for BC03,  $7.3_{7.1}^{7.4}$  for Z11, and  $6.2_{5.9}^{6.4}$  for the BPASS models. The nearly constant star formation assumed by **prospector** yields  $\log M_{\star}/M_{\odot} = 7.4_{7.3}^{7.5}$ . The difference between the median stellar mass for the  $z \sim 17$  and  $z \sim 25$  samples is 0.2-0.4 dex. Comparing these estimates with the dark matter halo masses obtained by using rank-preserving abundance matching shown in Figure 8, we obtain stellar-to-dark matter mass ratios around a few percent at  $z \sim 25$ , and 10 times smaller at  $z \sim 17$ .

Most of our galaxies show UV slopes and masses similar to the comparison samples (at  $10 \lesssim z \lesssim 12$ ) plotted in the figure (from Cullen et al. 2023, Austin et al. 2024, and Morales et al. 2024), which imply the presence of very young (1–10 Myr) stellar populations with significant nebular emission or older stars, resulting in slopes

around  $\beta \sim -2.5$ . Notably, we detect three galaxies with extreme UV colors ( $\beta \sim -3$ ), two at  $z \sim 17$  and one at  $z \sim 25$ . In fact, their SED is extremely blue and can only be reproduced with very young and metal-poor models (as anticipated in our discussion of Figure 8), as well as very small or negligible dust obscuration (e.g. Narayanan et al. 2025), and also including significant HeII $\lambda$ 1640 emission.

In fact, the SED of these extremely blue galaxies could only be fitted by switching off the nebular continuum emission, i.e., by assuming that the escape fraction of ionizing photons is low and the UV is dominated by stellar emission from very young and metal-poor stars with low dust content. This could be explained by the presence of strong bursts of star formation (as in the feedback-free burst models of Dekel et al. 2023) that quickly clear the inter-stellar medium, as suggested for the dust by Ferrara et al. (2023); Ferrara (2024).

Finally, we note that, except for the bluest galaxies, the UV slope of the  $z > 17$  candidates are generally consistent with those expected from the PopIII stellar systems observed at various stages of their initial bursts, as discussed by Katz et al. (2024). For age  $t < 10$  Myr, the predicted far UV emissivity and the slope of the continuum emission of these systems is the result of different proportions of stellar and nebular continuum, which is expected around  $\beta \approx -2.5$ , assuming stellar populations synthesis models and IMF as made here. Galaxies with the bluest UV continuum, i.e.,  $\beta \approx -3$ , would be consistent with this scenario only for IMF that include very massive stars or, as mentioned before, in presence of mechanisms capable to suppress the nebular continuum.

The average for the mass-weighted age according to the BC03 modeling is 44 Myr for the whole sample, 55 Myr for the  $z \sim 17$  subsample and 17 Myr for the  $z \sim 25$  sources, suggesting that the onset of the star formation in the  $z \sim 17$  ( $z \sim 25$ ) sample would be  $z_0 \sim 20$  ( $z_0 \sim 28$ ). These ages are similar to those obtained for spectroscopically confirmed galaxies at  $z = 10-14$  (Carniani et al. 2024; Helton et al. 2024; Zavala et al. 2025). With the Z11 models, we obtain mass-weighted ages 37, 44, and 21 Myr for the whole sample and the  $z \sim 17$  and  $z \sim 25$  selections respectively. For BPASS, the ages are significantly younger, all below 10 Myr. **prospector** obtains 60, 66 and 42 Myr for the whole sample and the  $z \sim 17$  and  $z \sim 25$  selections respectively. The stellar ages we obtain, combined with the information provided in Figure 8, imply that a star formation efficiency (i.e., mass in stars divided by mass in baryons) around 15% (that is assumed in Figure 8) matches well the observations at  $z \sim 17$ . This is consistent with the results re-

ported in, for example, Harikane et al. (2022) for lower redshifts (but still  $z \gtrsim 10$ ). For  $z \sim 25$ , since the ages are still not as young as the 1 Myr shown in Figure 8, we need  $\times 2 - 3$  times higher star formation efficiencies (around 40%).

The average attenuation is  $A(V) = 0.04$  mag for the whole sample and sub-samples for all SYNTHESIZER-AGN models. `prospector`, however, gives an average of  $A(V) = 0.3$  mag, as the constant SFH models need higher attenuations to fit the SEDs.

#### 4. SUMMARY AND CONCLUSIONS

With exposure times in broad-band NIRCcam filters between 33 and 90 hours in the common area, and 15 to 45 hours in non-overlapping regions, the combination of MIDIS and NGDEEP data provides the deepest JWST dataset to date, reaching  $5\sigma$  depths fainter than 31 mag. We utilize these data to search for  $z > 16$  galaxies identified as F200W and F277W dropouts.

We find six  $z \sim 17$  and three  $z \sim 25$  galaxy candidates, after a selection based on photometry, photometric redshift probability distributions, and visual inspection. The estimated average stellar masses for these sources are  $M_{\star}/M_{\odot} \sim 7.0$ , with mass-weighted stellar ages around 30 Myr, and very low dust content  $A(V) \sim 0.05$  mag. Typical UV spectral slopes are  $\beta \sim -2.5$ , with three galaxies presenting extremely blue values compatible with very metal-poor models, significant HeII $\lambda$ 1640 emission, and/or a low to negligible contribution to the UV emission from the nebular continuum that could be explained with high escape fractions of ionizing photons.

We construct UV luminosity functions and integrate them to get the cosmic luminosity density. Compared with results in the literature at  $z \leq 12$ , we find that the number density of galaxies around  $M_{UV} \sim -18.5$  mag decreases by a factor of  $\sim 4$  from  $z \sim 12$  to  $z \sim 17$  and a factor of  $\sim 25$  to  $z \sim 25$ . A similar evolution is observed for the luminosity density, which evolves proportional to  $(1+z)^{-5.3}$  at  $z \gtrsim 10$ . Compared to a compilation of recent galaxy evolution models (Dekel et al. 2023, Ferrara et al. 2023, Somerville et al. 2025), we find relatively good agreement up to  $z \sim 17$  with models in which the star formation efficiency was higher at early times. There are currently few robust predictions of the number density of galaxies at  $z \gtrsim 20$  in the literature, however, the continuing rapid drop in the comoving number density of halos that are above the atomic cooling limit ( $M_h \sim 10^7 M_{\odot}$  at  $z = 20$ ) suggests that an additional increase in the production efficiency of UV photons per unit halo mass may be required at  $z \gtrsim 17$ . This could be due to a higher conversion efficiency of gas into stars,

more efficient production of UV light per unit stellar mass (e.g. from stellar populations with a top heavy IMF), or a contribution to the UV light from accreting black holes.

Using an abundance matching technique, we infer that the galaxies we have selected as  $z \sim 17$  and  $z \sim 25$  candidates reside in  $M_{DM} = 10^{9.5} M_{\odot}$  and  $10^{8.5} M_{\odot}$  halos, respectively. Given that these galaxy populations have similar intrinsic rest-UV luminosities, this again suggests that the typical conversion efficiency of baryons into stars, or the photon production efficiency per unit stellar mass formed, or both, must have evolved to higher values over this time interval. Our analysis suggests typical mass-to-light ratios around  $10^{-6} M_{\odot}/L_{\odot}^{UV}$  for stellar masses, and  $10^{-4.5} M_{\odot}/L_{\odot}^{UV}$  for dark matter masses. Assuming that about 15% of the halo baryon budget has been turned into stars, these values are consistent with stellar population models with young ages (1-30 Myr) and low metallicities ( $< 0.1\% Z_{\odot}$ ).

Overall, our results indicate very rapid evolution of the formation of galaxies from  $z \sim 25$  to  $z \sim 12$ . This points to the epoch between 100 and 350 Myr after the Big Bang as the rise of the galaxy formation empire, when galaxies started to be ubiquitous in the Universe. From the observational point of view, our conclusion in this paper is that selecting robust galaxy candidates at  $z \sim 17$  and  $z \sim 25$  requires, given the strong evolution, reaching magnitudes in the selection bands (F277W and redder filters) of at least 31 mag,  $\sim 1.5$  mag deeper in the dropout filter (F200W and F277W), achievable with  $\geq 100$  hours integrations per band, expecting up to ten candidates per NIRCcam pointing.

We thank Andrea Ferrara and Brant Robertson for providing their latest simulation predictions and observational results for this paper, and Marco Castellano for useful discussions. P.G.P.-G. and L.C. acknowledge support from grant PID2022-139567NB-I00 funded by Spanish Ministerio de Ciencia e Innovación MCIN/AEI/10.13039/501100011033, FEDER *Una manera de hacer Europa*. This work has made use of the Rainbow Cosmological Surveys Database, which is operated by the Centro de Astrobiología (CAB), CSIC-INTA. The project that gave rise to these results received the support of a fellowship from the “la Caixa” Foundation (ID 100010434). The fellowship code is LCF/BQ/PR24/12050015. G.Ö. and J.M. acknowledges support from the Swedish National Space Agency (SNSA) and the Swedish Research Council (VR). L.C. and L.C. acknowledge support by grant PIB2021-127718NB-100 from the Spanish Ministry of Science and Innovation/State Agency of Research MCIN/AEI/10.13039/501100011033 and by “ERDF A way of making Europe”. This work was supported by research grants (VIL16599, VIL54489) from VILLUM FONDEN. P.N. acknowledges support from the Gordon and Betty Moore Foundation and the John Templeton Foundation that fund the Black Hole Initiative (BHI) at Harvard University. K.I.C. acknowledges funding from the Dutch Research Council (NWO) through the award of the Vici Grant VI.C.212.036 and funding from the Netherlands Research School for Astronomy (NOVA). The Cosmic Dawn Center (DAWN) is funded by the Danish National Research Foundation (DNRF) under grant No. 140. A.E. and F.P. acknowledge support through the German Space Agency DLR 50OS1501 and DLR 50OS2001 from 2015 to 2023. RSS is supported by the Flatiron Institute, which is operated by the Simons Foundation.

## REFERENCES

- Adamo, A., Atek, H., Bagley, M. B., et al. 2024, arXiv e-prints, arXiv:2405.21054, doi: [10.48550/arXiv.2405.21054](https://doi.org/10.48550/arXiv.2405.21054)
- Adams, N. J., Conselice, C. J., Austin, D., et al. 2024, ApJ, 965, 169, doi: [10.3847/1538-4357/ad2a7b](https://doi.org/10.3847/1538-4357/ad2a7b)
- Akhlaghi, M., & Ichikawa, T. 2015, ApJS, 220, 1, doi: [10.1088/0067-0049/220/1/1](https://doi.org/10.1088/0067-0049/220/1/1)
- Arrabal Haro, P., Dickinson, M., Finkelstein, S. L., et al. 2023a, Nature, 622, 707, doi: [10.1038/s41586-023-06521-7](https://doi.org/10.1038/s41586-023-06521-7)
- . 2023b, ApJL, 951, L22, doi: [10.3847/2041-8213/acdd54](https://doi.org/10.3847/2041-8213/acdd54)
- Austin, D., Conselice, C. J., Adams, N. J., et al. 2024, arXiv e-prints, arXiv:2404.10751, doi: [10.48550/arXiv.2404.10751](https://doi.org/10.48550/arXiv.2404.10751)
- Bagley, M. B., Finkelstein, S. L., Koekemoer, A. M., et al. 2023, ApJL, 946, L12, doi: [10.3847/2041-8213/acbb08](https://doi.org/10.3847/2041-8213/acbb08)
- Bagley, M. B., Pirzkal, N., Finkelstein, S. L., et al. 2024, ApJL, 965, L6, doi: [10.3847/2041-8213/ad2f31](https://doi.org/10.3847/2041-8213/ad2f31)
- Behroozi, P. S., Conroy, C., & Wechsler, R. H. 2010, ApJ, 717, 379, doi: [10.1088/0004-637X/717/1/379](https://doi.org/10.1088/0004-637X/717/1/379)
- Behroozi, P. S., Wechsler, R. H., & Conroy, C. 2013, ApJ, 770, 57, doi: [10.1088/0004-637X/770/1/57](https://doi.org/10.1088/0004-637X/770/1/57)

- Beiler, S. A., Cushing, M. C., Kirkpatrick, J. D., et al. 2023, *ApJL*, 951, L48, doi: [10.3847/2041-8213/ace32c](https://doi.org/10.3847/2041-8213/ace32c)
- Bertin, E., & Arnouts, S. 1996, *A&AS*, 117, 393, doi: [10.1051/aas:1996164](https://doi.org/10.1051/aas:1996164)
- Bezanson, R., Labbe, I., Whitaker, K. E., et al. 2024, *ApJ*, 974, 92, doi: [10.3847/1538-4357/ad66cf](https://doi.org/10.3847/1538-4357/ad66cf)
- Bhowmick, A. K., Somerville, R. S., Di Matteo, T., et al. 2020, *MNRAS*, 496, 754, doi: [10.1093/mnras/staa1605](https://doi.org/10.1093/mnras/staa1605)
- Bouwens, R., Illingworth, G., Oesch, P., et al. 2022a, arXiv e-prints, arXiv:2212.06683. <https://arxiv.org/abs/2212.06683>
- Bouwens, R. J., Stefanon, M., Brammer, G., et al. 2022b, arXiv e-prints, arXiv:2211.02607, doi: [10.48550/arXiv.2211.02607](https://doi.org/10.48550/arXiv.2211.02607)
- Brammer, G. B., van Dokkum, P. G., & Coppi, P. 2008, *ApJ*, 686, 1503, doi: [10.1086/591786](https://doi.org/10.1086/591786)
- Bruzual, G., & Charlot, S. 2003, *MNRAS*, 344, 1000, doi: [10.1046/j.1365-8711.2003.06897.x](https://doi.org/10.1046/j.1365-8711.2003.06897.x)
- Calzetti, D., Armus, L., Bohlin, R. C., et al. 2000, *ApJ*, 533, 682, doi: [10.1086/308692](https://doi.org/10.1086/308692)
- Carniani, S., Hainline, K., D'Eugenio, F., et al. 2024, *Nature*, 633, 318, doi: [10.1038/s41586-024-07860-9](https://doi.org/10.1038/s41586-024-07860-9)
- Casey, C. M., Kartaltepe, J. S., Drakos, N. E., et al. 2023, *ApJ*, 954, 31, doi: [10.3847/1538-4357/acc2bc](https://doi.org/10.3847/1538-4357/acc2bc)
- Casey, C. M., Akins, H. B., Shuntov, M., et al. 2024, *ApJ*, 965, 98, doi: [10.3847/1538-4357/ad2075](https://doi.org/10.3847/1538-4357/ad2075)
- Castellano, M., Fontana, A., Treu, T., et al. 2022, *ApJL*, 938, L15, doi: [10.3847/2041-8213/ac94d0](https://doi.org/10.3847/2041-8213/ac94d0)
- . 2023, *ApJL*, 948, L14, doi: [10.3847/2041-8213/accea5](https://doi.org/10.3847/2041-8213/accea5)
- Castellano, M., Napolitano, L., Fontana, A., et al. 2024, *ApJ*, 972, 143, doi: [10.3847/1538-4357/ad5f88](https://doi.org/10.3847/1538-4357/ad5f88)
- Chabrier, G. 2003, *PASP*, 115, 763, doi: [10.1086/376392](https://doi.org/10.1086/376392)
- Conroy, C., & Gunn, J. E. 2010, *FSPS: Flexible Stellar Population Synthesis*, Astrophysics Source Code Library, record ascl:1010.043. <http://ascl.net/1010.043>
- Conselice, C. J., Adams, N., Harvey, T., et al. 2024, arXiv e-prints, arXiv:2407.14973, doi: [10.48550/arXiv.2407.14973](https://doi.org/10.48550/arXiv.2407.14973)
- Cullen, F., McLure, R. J., McLeod, D. J., et al. 2023, *MNRAS*, 520, 14, doi: [10.1093/mnras/stad073](https://doi.org/10.1093/mnras/stad073)
- Curti, M., D'Eugenio, F., Carniani, S., et al. 2023, *MNRAS*, 518, 425, doi: [10.1093/mnras/stac2737](https://doi.org/10.1093/mnras/stac2737)
- Curtis-Lake, E., Carniani, S., Cameron, A., et al. 2023, *Nature Astronomy*, 7, 622, doi: [10.1038/s41550-023-01918-w](https://doi.org/10.1038/s41550-023-01918-w)
- Dekel, A., Sarkar, K. C., Birnboim, Y., Mandelker, N., & Li, Z. 2023, *MNRAS*, 523, 3201, doi: [10.1093/mnras/stad1557](https://doi.org/10.1093/mnras/stad1557)
- Donnan, C. T., McLeod, D. J., Dunlop, J. S., et al. 2023, *MNRAS*, 518, 6011, doi: [10.1093/mnras/stac3472](https://doi.org/10.1093/mnras/stac3472)
- Donnan, C. T., McLure, R. J., Dunlop, J. S., et al. 2024, *MNRAS*, 533, 3222, doi: [10.1093/mnras/stae2037](https://doi.org/10.1093/mnras/stae2037)
- Efstathiou, G., Ellis, R. S., & Peterson, B. A. 1988, *MNRAS*, 232, 431, doi: [10.1093/mnras/232.2.431](https://doi.org/10.1093/mnras/232.2.431)
- Eisenstein, D. J., Willott, C., Alberts, S., et al. 2023, arXiv e-prints, arXiv:2306.02465, doi: [10.48550/arXiv.2306.02465](https://doi.org/10.48550/arXiv.2306.02465)
- Eldridge, J. J., Stanway, E. R., Xiao, L., et al. 2017, *PASA*, 34, e058, doi: [10.1017/pasa.2017.51](https://doi.org/10.1017/pasa.2017.51)
- Erb, D. K., Pettini, M., Shapley, A. E., et al. 2010, *ApJ*, 719, 1168, doi: [10.1088/0004-637X/719/2/1168](https://doi.org/10.1088/0004-637X/719/2/1168)
- Ferrara, A. 2024, *A&A*, 689, A310, doi: [10.1051/0004-6361/202450944](https://doi.org/10.1051/0004-6361/202450944)
- Ferrara, A., Pallottini, A., & Dayal, P. 2023, *MNRAS*, 522, 3986, doi: [10.1093/mnras/stad1095](https://doi.org/10.1093/mnras/stad1095)
- Finkelstein, S. L., Bagley, M. B., Arrabal Haro, P., et al. 2022, *ApJL*, 940, L55, doi: [10.3847/2041-8213/ac966e](https://doi.org/10.3847/2041-8213/ac966e)
- Finkelstein, S. L., Bagley, M. B., Ferguson, H. C., et al. 2023, *ApJL*, 946, L13, doi: [10.3847/2041-8213/acade4](https://doi.org/10.3847/2041-8213/acade4)
- Finkelstein, S. L., Leung, G. C. K., Bagley, M. B., et al. 2024, *ApJL*, 969, L2, doi: [10.3847/2041-8213/ad4495](https://doi.org/10.3847/2041-8213/ad4495)
- Finkelstein, S. L., Bagley, M. B., Arrabal Haro, P., et al. 2025, arXiv e-prints, arXiv:2501.04085, doi: [10.48550/arXiv.2501.04085](https://doi.org/10.48550/arXiv.2501.04085)
- Foreman-Mackey, D., Sick, J., & Johnson, B. 2014, *python-fsps: Python bindings to FSPS (v0.1.1)*, v0.1.1, Zenodo, doi: [10.5281/zenodo.12157](https://doi.org/10.5281/zenodo.12157)
- Gaia Collaboration, Prusti, T., de Bruijne, J. H. J., et al. 2016a, *A&A*, 595, A1, doi: [10.1051/0004-6361/201629272](https://doi.org/10.1051/0004-6361/201629272)
- Gaia Collaboration, Brown, A. G. A., Vallenari, A., et al. 2016b, *A&A*, 595, A2, doi: [10.1051/0004-6361/201629512](https://doi.org/10.1051/0004-6361/201629512)
- Golini, G., Montes, M., Carrasco, E. R., Román, J., & Trujillo, I. 2024, *A&A*, 684, A99, doi: [10.1051/0004-6361/202348300](https://doi.org/10.1051/0004-6361/202348300)
- Hainline, K. N., Johnson, B. D., Robertson, B., et al. 2024a, *ApJ*, 964, 71, doi: [10.3847/1538-4357/ad1ee4](https://doi.org/10.3847/1538-4357/ad1ee4)
- Hainline, K. N., Helton, J. M., Johnson, B. D., et al. 2024b, *ApJ*, 964, 66, doi: [10.3847/1538-4357/ad20d1](https://doi.org/10.3847/1538-4357/ad20d1)
- Harikane, Y., Nakajima, K., Ouchi, M., et al. 2024, *ApJ*, 960, 56, doi: [10.3847/1538-4357/ad0b7e](https://doi.org/10.3847/1538-4357/ad0b7e)
- Harikane, Y., Ono, Y., Ouchi, M., et al. 2022, *ApJS*, 259, 20, doi: [10.3847/1538-4365/ac3dfc](https://doi.org/10.3847/1538-4365/ac3dfc)
- Harikane, Y., Ouchi, M., Oguri, M., et al. 2023, *ApJS*, 265, 5, doi: [10.3847/1538-4365/acaaa9](https://doi.org/10.3847/1538-4365/acaaa9)
- Helton, J. M., Rieke, G. H., Alberts, S., et al. 2024, arXiv e-prints, arXiv:2405.18462, doi: [10.48550/arXiv.2405.18462](https://doi.org/10.48550/arXiv.2405.18462)
- Johnson, B. D., Leja, J., Conroy, C., & Speagle, J. S. 2021, *ApJS*, 254, 22, doi: [10.3847/1538-4365/abef67](https://doi.org/10.3847/1538-4365/abef67)

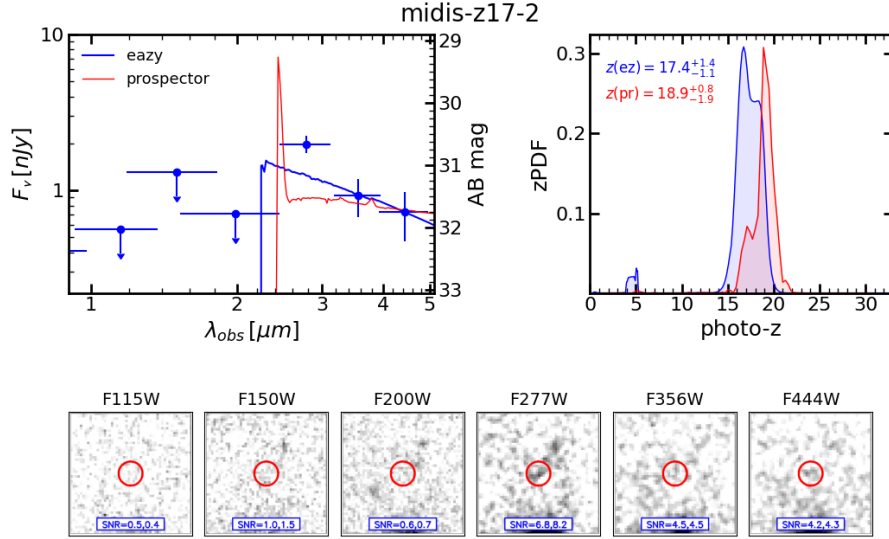
- Katz, H., Cameron, A. J., Saxena, A., et al. 2024, arXiv e-prints, arXiv:2408.03189, doi: [10.48550/arXiv.2408.03189](https://doi.org/10.48550/arXiv.2408.03189)
- Killi, M., Watson, D., Brammer, G., et al. 2023, arXiv e-prints, arXiv:2312.03065, doi: [10.48550/arXiv.2312.03065](https://doi.org/10.48550/arXiv.2312.03065)
- Kokorev, V., Atek, H., Chisholm, J., et al. 2024, arXiv e-prints, arXiv:2411.13640, doi: [10.48550/arXiv.2411.13640](https://doi.org/10.48550/arXiv.2411.13640)
- Kron, R. G. 1980, *ApJS*, 43, 305, doi: [10.1086/190669](https://doi.org/10.1086/190669)
- Kroupa, P. 2001, *MNRAS*, 322, 231, doi: [10.1046/j.1365-8711.2001.04022.x](https://doi.org/10.1046/j.1365-8711.2001.04022.x)
- Larson, R. L., Hutchison, T. A., Bagley, M., et al. 2022, arXiv e-prints, arXiv:2211.10035, <https://arxiv.org/abs/2211.10035>
- Lei, L., Wang, Y.-Y., Yuan, G.-W., et al. 2025, *ApJ*, 980, 249, doi: [10.3847/1538-4357/ada93b](https://doi.org/10.3847/1538-4357/ada93b)
- Leung, G. C. K., Bagley, M. B., Finkelstein, S. L., et al. 2023, *ApJL*, 954, L46, doi: [10.3847/2041-8213/acf365](https://doi.org/10.3847/2041-8213/acf365)
- Li, Z., Dekel, A., Sarkar, K. C., et al. 2024, *A&A*, 690, A108, doi: [10.1051/0004-6361/202348727](https://doi.org/10.1051/0004-6361/202348727)
- McLeod, D. J., Donnan, C. T., McLure, R. J., et al. 2024, *MNRAS*, 527, 5004, doi: [10.1093/mnras/stad3471](https://doi.org/10.1093/mnras/stad3471)
- Menon, S. H., Lancaster, L., Burkhart, B., et al. 2024, *ApJL*, 967, L28, doi: [10.3847/2041-8213/ad462d](https://doi.org/10.3847/2041-8213/ad462d)
- Morales, A. M., Finkelstein, S. L., Leung, G. C. K., et al. 2024, *ApJL*, 964, L24, doi: [10.3847/2041-8213/ad2de4](https://doi.org/10.3847/2041-8213/ad2de4)
- Morishita, T., Mason, C. A., Kreilgaard, K. C., et al. 2024, arXiv e-prints, arXiv:2412.04211, doi: [10.48550/arXiv.2412.04211](https://doi.org/10.48550/arXiv.2412.04211)
- Muzzin, A., Marchesini, D., Stefanon, M., et al. 2013, *ApJS*, 206, 8, doi: [10.1088/0067-0049/206/1/8](https://doi.org/10.1088/0067-0049/206/1/8)
- Naidu, R. P., Oesch, P. A., Setton, D. J., et al. 2022, arXiv e-prints, arXiv:2208.02794, doi: [10.48550/arXiv.2208.02794](https://doi.org/10.48550/arXiv.2208.02794)
- Nakajima, K., Ouchi, M., Isobe, Y., et al. 2023, *ApJS*, 269, 33, doi: [10.3847/1538-4365/acd556](https://doi.org/10.3847/1538-4365/acd556)
- Narayanan, D., Stark, D. P., Finkelstein, S. L., et al. 2025, *ApJ*, 982, 7, doi: [10.3847/1538-4357/adb41c](https://doi.org/10.3847/1538-4357/adb41c)
- Oesch, P. A., Bouwens, R. J., Illingworth, G. D., Labbé, I., & Stefanon, M. 2018, *ApJ*, 855, 105, doi: [10.3847/1538-4357/aab03f](https://doi.org/10.3847/1538-4357/aab03f)
- Oke, J. B., & Gunn, J. E. 1983, *ApJ*, 266, 713, doi: [10.1086/160817](https://doi.org/10.1086/160817)
- Östlin, G., Pérez-González, P. G., Melinder, J., et al. 2024, arXiv e-prints, arXiv:2411.19686, doi: [10.48550/arXiv.2411.19686](https://doi.org/10.48550/arXiv.2411.19686)
- Pérez-González, P. G., Gil de Paz, A., Zamorano, J., et al. 2003, *MNRAS*, 338, 508, doi: [10.1046/j.1365-8711.2003.06077.x](https://doi.org/10.1046/j.1365-8711.2003.06077.x)
- Pérez-González, P. G., Rieke, G. H., Villar, V., et al. 2008, *ApJ*, 675, 234, doi: [10.1086/523690](https://doi.org/10.1086/523690)
- Pérez-González, P. G., Costantin, L., Langeroodi, D., et al. 2023a, *ApJL*, 951, L1, doi: [10.3847/2041-8213/acd9d0](https://doi.org/10.3847/2041-8213/acd9d0)
- Pérez-González, P. G., Barro, G., Annunziatella, M., et al. 2023b, *ApJL*, 946, L16, doi: [10.3847/2041-8213/acb3a5](https://doi.org/10.3847/2041-8213/acb3a5)
- Pérez-González, P. G., Barro, G., Rieke, G. H., et al. 2024, *ApJ*, 968, 4, doi: [10.3847/1538-4357/ad38bb](https://doi.org/10.3847/1538-4357/ad38bb)
- Rieke, M. J., Robertson, B., Tacchella, S., et al. 2023, *ApJS*, 269, 16, doi: [10.3847/1538-4365/acf44d](https://doi.org/10.3847/1538-4365/acf44d)
- Rix, H.-W., Barden, M., Beckwith, S. V. W., et al. 2004, *ApJS*, 152, 163, doi: [10.1086/420885](https://doi.org/10.1086/420885)
- Robertson, B., Johnson, B. D., Tacchella, S., et al. 2024, *ApJ*, 970, 31, doi: [10.3847/1538-4357/ad463d](https://doi.org/10.3847/1538-4357/ad463d)
- Robertson, B. E., Tacchella, S., Johnson, B. D., et al. 2023, *Nature Astronomy*, 7, 611, doi: [10.1038/s41550-023-01921-1](https://doi.org/10.1038/s41550-023-01921-1)
- Sanders, R. L., Shapley, A. E., Topping, M. W., Reddy, N. A., & Brammer, G. B. 2024, *ApJ*, 962, 24, doi: [10.3847/1538-4357/ad15fc](https://doi.org/10.3847/1538-4357/ad15fc)
- Schechter, P. 1976, *ApJ*, 203, 297, doi: [10.1086/154079](https://doi.org/10.1086/154079)
- Somerville, R. S., Hopkins, P. F., Cox, T. J., Robertson, B. E., & Hernquist, L. 2008, *MNRAS*, 391, 481, doi: [10.1111/j.1365-2966.2008.13805.x](https://doi.org/10.1111/j.1365-2966.2008.13805.x)
- Speagle, J. S. 2020, *MNRAS*, 493, 3132, doi: [10.1093/mnras/staa278](https://doi.org/10.1093/mnras/staa278)
- Tinker, J., Kravtsov, A. V., Klypin, A., et al. 2008, *ApJ*, 688, 709, doi: [10.1086/591439](https://doi.org/10.1086/591439)
- Trapp, A. C., & Furlanetto, S. R. 2020, *MNRAS*, 499, 2401, doi: [10.1093/mnras/staa2828](https://doi.org/10.1093/mnras/staa2828)
- Trenti, M., & Stiavelli, M. 2008, *ApJ*, 676, 767, doi: [10.1086/528674](https://doi.org/10.1086/528674)
- Trujillo-Gomez, S., Klypin, A., Primack, J., & Romanowsky, A. J. 2011, *ApJ*, 742, 16, doi: [10.1088/0004-637X/742/1/16](https://doi.org/10.1088/0004-637X/742/1/16)
- Trump, J. R., Arrabal Haro, P., Simons, R. C., et al. 2023, *ApJ*, 945, 35, doi: [10.3847/1538-4357/acba8a](https://doi.org/10.3847/1538-4357/acba8a)
- Ucci, G., Dayal, P., Hutter, A., et al. 2021, *MNRAS*, 506, 202, doi: [10.1093/mnras/stab1229](https://doi.org/10.1093/mnras/stab1229)
- Whitaker, K. E., Ashas, M., Illingworth, G., et al. 2019, *ApJS*, 244, 16, doi: [10.3847/1538-4365/ab3853](https://doi.org/10.3847/1538-4365/ab3853)
- Whitler, L., Stark, D. P., Topping, M. W., et al. 2025, arXiv e-prints, arXiv:2501.00984, doi: [10.48550/arXiv.2501.00984](https://doi.org/10.48550/arXiv.2501.00984)
- Willmer, C. N. A. 2018, *ApJS*, 236, 47, doi: [10.3847/1538-4365/aabfdff](https://doi.org/10.3847/1538-4365/aabfdff)
- Willott, C. J., Desprez, G., Asada, Y., et al. 2024, *ApJ*, 966, 74, doi: [10.3847/1538-4357/ad35bc](https://doi.org/10.3847/1538-4357/ad35bc)
- Yan, H., Ma, Z., Ling, C., Cheng, C., & Huang, J.-S. 2023a, *ApJL*, 942, L9, doi: [10.3847/2041-8213/aca80c](https://doi.org/10.3847/2041-8213/aca80c)

- Yan, H., Sun, B., Ma, Z., & Ling, C. 2023b, arXiv e-prints, arXiv:2311.15121, doi: [10.48550/arXiv.2311.15121](https://doi.org/10.48550/arXiv.2311.15121)
- Yan, H., Cohen, S. H., Windhorst, R. A., et al. 2023c, ApJL, 942, L8, doi: [10.3847/2041-8213/aca974](https://doi.org/10.3847/2041-8213/aca974)
- Yung, L. Y. A., Somerville, R. S., Finkelstein, S. L., Wilkins, S. M., & Gardner, J. P. 2024a, MNRAS, 527, 5929, doi: [10.1093/mnras/stad3484](https://doi.org/10.1093/mnras/stad3484)
- Yung, L. Y. A., Somerville, R. S., Nguyen, T., et al. 2024b, MNRAS, 530, 4868, doi: [10.1093/mnras/stae1188](https://doi.org/10.1093/mnras/stae1188)
- Zackrisson, E., Rydberg, C.-E., Schaerer, D., Östlin, G., & Tuli, M. 2011, ApJ, 740, 13, doi: [10.1088/0004-637X/740/1/13](https://doi.org/10.1088/0004-637X/740/1/13)
- Zavala, J. A., Buat, V., Casey, C. M., et al. 2022, arXiv e-prints, arXiv:2208.01816, doi: [10.48550/arXiv.2208.01816](https://doi.org/10.48550/arXiv.2208.01816)
- . 2023, ApJL, 943, L9, doi: [10.3847/2041-8213/acacfe](https://doi.org/10.3847/2041-8213/acacfe)
- Zavala, J. A., Castellano, M., Akins, H. B., et al. 2025, Nature Astronomy, 9, 155, doi: [10.1038/s41550-024-02397-3](https://doi.org/10.1038/s41550-024-02397-3)

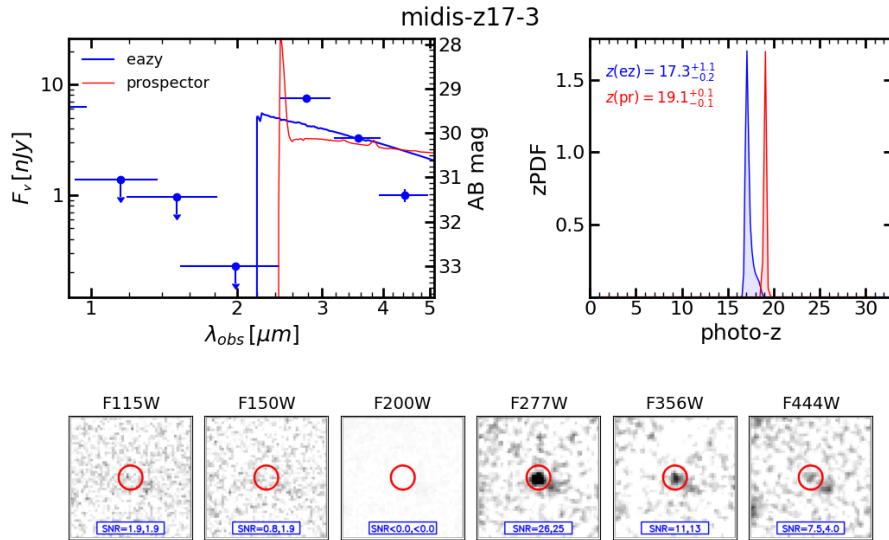
## APPENDIX

## A. HIGH REDSHIFT GALAXY CANDIDATES

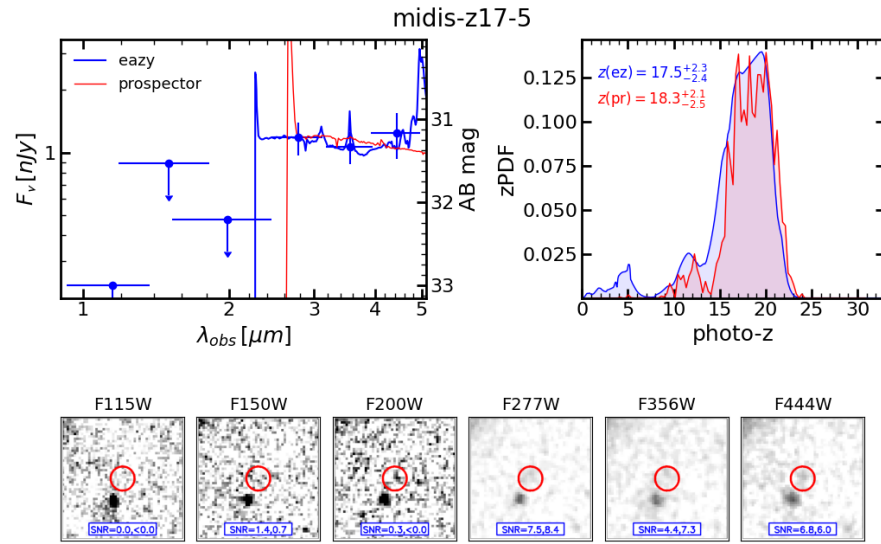
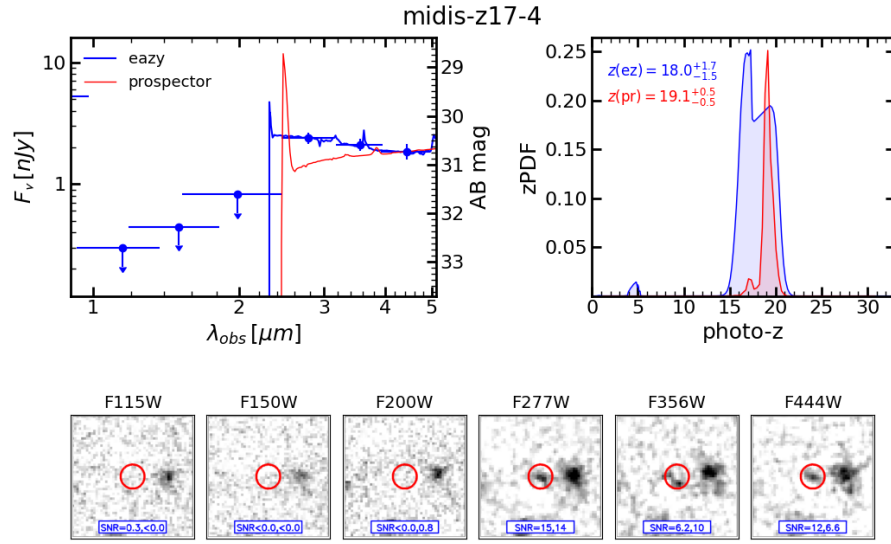
In the following figures, we show the SED fits, zPDFs, and postage stamps of the galaxy candidates at  $z \sim 17$  (Figures 10, 11, 12, 13, and 14) and at  $z \sim 24$  (Figures 15 and 16).



**Figure 10.** One of the galaxies selected in the  $z \sim 17$  sample. The figure shows the same information depicted for an example galaxy in the main text (Figure 3).



**Figure 11.** Same as Figure 10 for another galaxy selected in the  $z \sim 17$  sample.





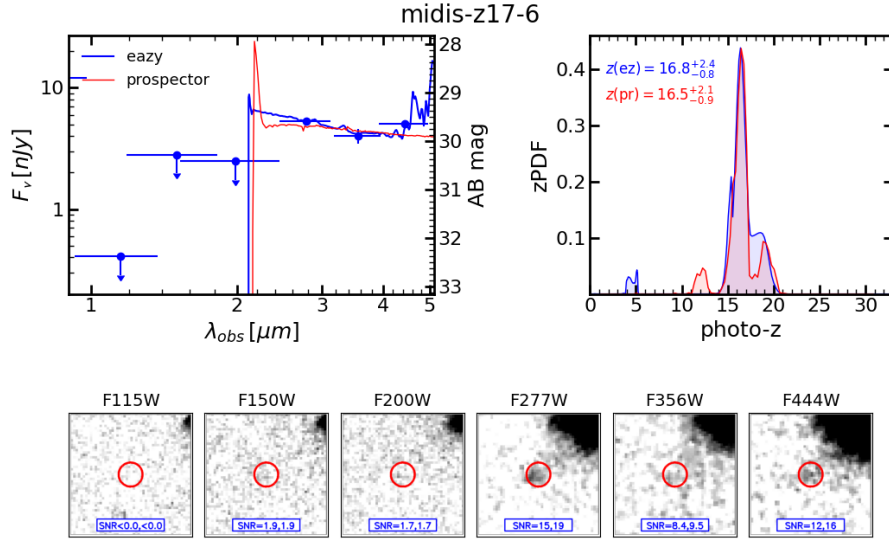


Figure 14. Same as Figure 10 for another galaxy selected in the  $z \sim 17$  sample.

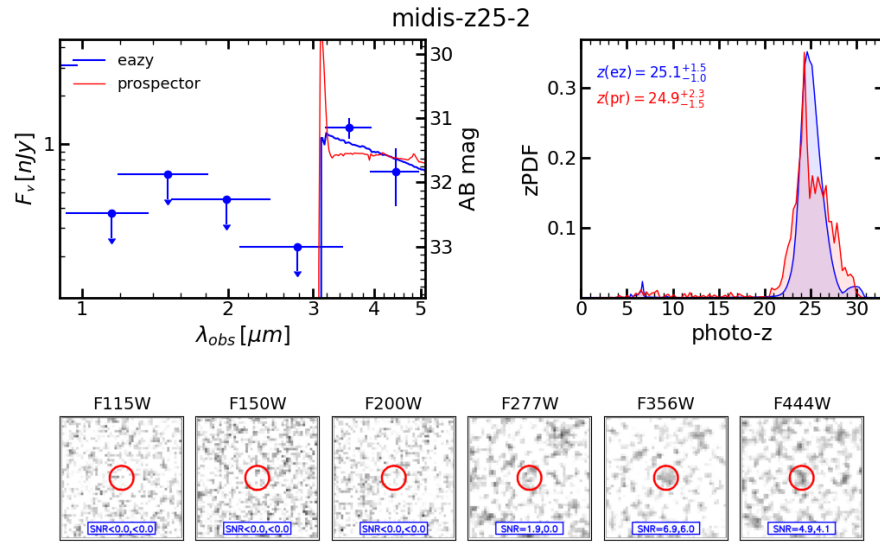
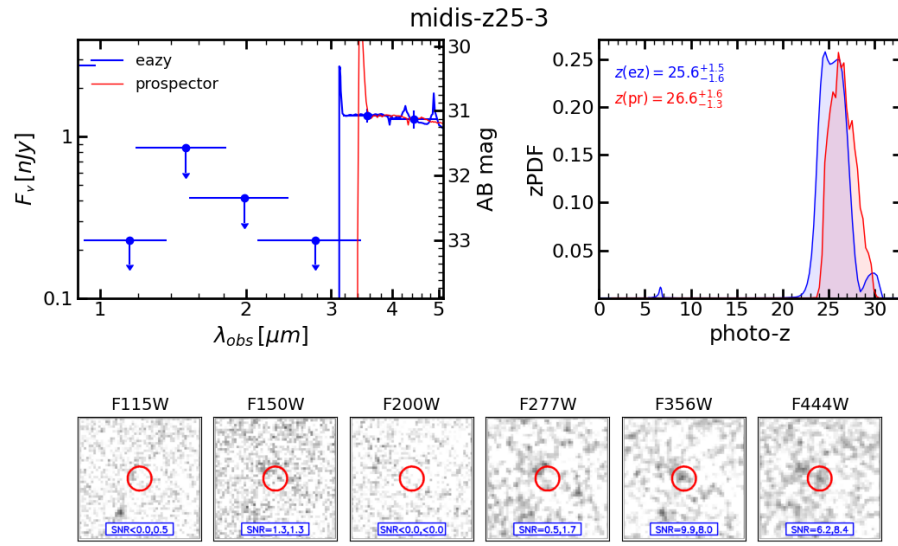


Figure 15. One of the galaxies selected in the  $z \sim 24$  sample. The figure shows the same information depicted for an example galaxy in the main text (Figure 3).



**Figure 16.** Same as Figure 15 for another galaxy selected in the  $z \sim 24$  sample.

## B. OTHER HIGH REDSHIFT GALAXY CANDIDATES

In the following Table 6, we list sources that were in the border of one of our selection criteria and were finally excluded from the luminosity function and subsequent calculations. We list their coordinates, the inferred approximate photometric redshifts, and the reason to discard them.

**Table 6.** Other galaxy candidates at  $14 < z < 25$ .

MIDIS ID	RA (J2000) [degrees]	DEC (J2000) [degrees]	redshift	Reason to discard
midisred0078692	53.31222420	-27.88696470	$z \sim 17$	$r = 0.1''$ aperture gives $z \sim 5$
midisred0007023	53.29276170	-27.87913810	$z \sim 24$	$r = 0.2''$ aperture gives $z \sim 8$
midisred0008188	53.25742490	-27.87752330	$z \sim 17$	$r = 0.1''$ gives $SNR = 2$ for SW images stacks
midisred0081800	53.27634280	-27.87423430	$z \sim 17$	$r = 0.1''$ gives $SNR = 2$ for SW images stacks
midisred0022529	53.30681440	-27.86221840	$z \sim 22$	$r = 0.1''$ aperture gives $z \sim 16$
midisred0045193	53.25118440	-27.82049580	$z \sim 16$	$r = 0.1''$ aperture gives $z \sim 5$
midisred0075426	53.26640900	-27.81979570	$z \sim 25$	in the limit of the $SNR = 5$ cut
midisred0075755	53.25900040	-27.81663240	$z \sim 25$	in the limit of the $SNR = 5$ cut
midisred0054262	53.24777980	-27.79423420	$z \sim 14$	$r = 0.2''$ aperture gives $z \sim 5$ , nearby bright source